UNIVERSIDADE ESTADUAL PAULISTA
"JULIO DE MESQUITA FILHO"

CAMPUS DE BOTUCATU – INSTITUTO DE BIOCIENCIAS

Avaliação da dinâmica hepática por Biosusceptometria AC e biodistribuição de nanopartículas magnéticas

GUILHERME AUGUSTO SOARES

Botucatu
2022

UNIVERSIDADE ESTADUAL PAULISTA
"JÚLIO DE MESQUITA FILHO"

PROGRAMA DE PÓS-GRADUAÇÃO EM
FARMACOLOGIA E BIOTECNOLOGIA
(PPG-FARMATEC)

Instituto de Biociências
de Botucatu - Unesp

Avaliação da dinâmica hepática por Biosusceptometria AC e biodistribuição de nanopartículas magnéticas

GUILHERME AUGUSTO SOARES

Tese de doutorado apresentada ao Instituto de Biociências, Universidade Estadual Paulista "Júlio de Mesquita Filho", Câmpus de Botucatu para obtenção do Título de Doutor em Farmacologia e Biotecnologia.

Orientador: Prof. Dr. José Ricardo de Arruda Miranda

Botucatu
2022

FICHA CATALOGRÁFICA ELABORADA PELA SEÇÃO TÉC. AQUIS. TRATAMENTO DA INFORM.
DIVISÃO TÉCNICA DE BIBLIOTECA E DOCUMENTAÇÃO - CÂMPUS DE BOTUCATU - UNESP
BIBLIOTECÁRIA RESPONSÁVEL: ROSEMEIRE APARECIDA VICENTE-CRB 8/5651

Soares, Guilherme Augusto.
Avaliação da dinâmica hepática por Biosusceptometria AC e biodistribuição de nanopartículas magnéticas / Guilherme Augusto Soares. - Botucatu, 2022

Tese (doutorado) - Universidade Estadual Paulista "Júlio de Mesquita Filho", Instituto de Biociências de Botucatu
Orientador: Josér Ricardo de Arruda Miranda
Capes: 20903006

1. Biosusceptometria de Corrente Alternada. 2. Fígado. 3. Nanotecnologia. 4. Nanoparticulas. 5. Testes de função hepática.

Palavras-chave: Biosusceptometria AC; Fígado; Imagem; Nanoparticulas magnéticas; Nanotecnologia.

Dedico esse trabalho a duas pessoas especiais: Helena Rezende Soares, que muita alegria continua nos trazendo, e à minha querida Gabriela Siqueira Peres, que nunca mediu esforços para proporcionar alegria à Helena.

“O que eu espero senhores, é que depois de um razoável período de discussão, todo mundo concorde comigo.”

Winston Churchill

AGRADECIMENTOS

Em primeiro lugar, gostaria de agradecer a Deus por sempre estar de alguma forma comigo em momentos bons e principalmente nos difíceis.

Agradeço aos meus pais, Luiz Antônio Soares e Maria Célia de Freitas, por nunca deixarem meus desânimos e devaneios tomarem conta e me desestabilizar. Gostaria de demonstrar todo meu carinho através da realização desse trabalho, que vem finalizar uma etapa se iniciou desde o meu ingresso na UNESP em 2012, e que o esforço e a luta de cada um foram o maior incentivo para mim. Agradeço a meus irmãos Luiz Felipe e Leonardo, que sempre estiveram ao meu lado, os quais considero meus ídolos e exemplos de homens, que sempre serão meu porto seguro e minha felicidade reservada.

Agradeço especialmente a minha doce Gabriela Siqueira Peres que me mostrou que não importa onde estejamos e quão longe os caminhos possam nos levar, não precisaremos de escudos, pois o amor é a armadura que precisamos e juntos somos invencíveis. Agradeço imensamente a Maria Dirce Botelho, Solange Siqueira, Carolina Siqueira e Bruno Siqueira por me terem como família desde o início. Deixo meu agradecimento especial à Solange, que durante essa etapa final ajudou como um filho.

Agradeço especialmente a meu orientador José Ricardo de Arruda Miranda, por atuar mais do que um simples orientador, e sim como um conselheiro, permitindo-me alcançar tudo que conquistei até agora, e que talvez sem o seu apoio, nada seria possível. Gostaria de agradecer a Prof. Diana Miranda Pina por me auxiliar em vários momentos e proporcionar um ambiente familiar ao laboratório.

Agradeço ao meu grande amigo André Gonçalves Próspero por todo companheirismo e ensinamentos que me proporcionou desde o início de minha trajetória até nosso período na Alemanha. Serei sempre grato por ter me auxiliando durante esses anos de maneira incrível. Gostaria de agradecer a outro importante amigo que é Leonardo Antônio Pinto, por me ajudar em inúmeras situações e sempre por nossas conversas.

Agradeço aos amigos do Physikalisch-Technische Bundesanstalt, em especial a Maik Liebl por me ajudar em inúmeras situações, e nunca medir esforços para me auxiliar em situações acadêmicas como cotidianas. Agradeço ao Dr. Frank Wiekhorst por me receberem tão bem em Berlim e por participar de uma etapa tão importante em minha

minha vida. Seguramente sem os dois nada seria possível. Agradeço também a Patricia Radon e Soudabeh Arsalani por tudo suporte oferecido em minha estadia no PTB.

Agradeço a Gabriele Martins Pereira por toda ajuda nessa etapa do doutorado e por ter sido uma grande companheira de laboratório, a quem acredito que irá alcançar um futuro brilhante.

Agradeço aos amigos Erick Guilherme Stoppa e João Miguel Barboza pelos momentos que pudemos compartilhar nesses últimos anos e por nossa amizade. Espero tê-los como grandes amigos por muito tempo. E agradeço ao meu primeiro co-orientador Caio Cesar Quini, que me direcionou no começo da minha trajetória na vida acadêmica.

Aos meus amigos Luan Adriano, Diego Franco, Felipe Morais, Otávio Bertoto, Paulo Otavio, Paulo Gabriel pela nossa longa amizade que de certa forma me ajudou até agora. Agradeço especialmente a Vinicius Bertoto por todo apoio em momentos difíceis que vivenciei.

Aos amigos da república RT, que através de companheirismo e muita alegria momentos difíceis eram contornados. Em especial, a quem tive mais contato: Diego Marcelino, Gabriel Perez, Mateus Pontim, Kayque Fracarolli, Inaiã Vieira, Vitor Hugo, Hugo Tadashi, Rodolfo Cicolin, Rafael Gelaleti, Pedro Pellicano e Bruno Gomes.

O presente trabalho foi realizado com apoio da Coordenação de Aperfeiçoamento de Pessoal de Nível Superior – Brasil (CAPES) – Código de Financiamento 88882.432964/2019-01 e 88887.657628/2021-00.

A todos que de forma direta e indireta participaram da realização desse trabalho como em minha vida, meu grande obrigado.

RESUMO

A presente tese de doutorado inclui resultados de trabalhos que foram realizados em estudos envolvendo a técnica de Biosusceptometria AC (BAC) e nanopartículas magnéticas (NPMs). A partir de uma sequência de trabalhos utilizando NPMs, os resultados aqui apresentados são passos importantes para compressão de parâmetros fisiológicos do sistema biológico como de parâmetros farmacocinéticos para as NPMs. O enfoque de ambos os trabalhos é uma avaliação direcionada ao fígado, considerado o principal órgão responsável pela captura de NPMs da corrente sanguínea. O primeiro trabalho a ser exibido nesse documento é uma avaliação de tempo longo, na qual foi investigado por 60 dias o perfil de acumulo e distribuição de NPMs administradas intravenosamente. Nesse estudo, os resultados indicaram uma maior captação pelo fígado e pelo baço devido às suas características de retenção e captação. Em 60 dias, observou-se ausência de NPMs no baço e uma deterioração significativa no fígado. Os dados indicaram um perfil de decaimento da concentração ao longo dos 60 dias, o que sugere que, além da eliminação pelas fezes, existe um mecanismo endógeno de metabolização ou possível aglomeração de NPMs, o que resulta em perda da intensidade do sinal BAC.

Uma vez que as NPMs apresentam a possibilidade de serem usadas como sondas multifuncionais para diagnóstico e tratamento nos últimos anos de doenças hepáticas, no segundo trabalho objetivou-se avaliar como a condição de cirrose influencia e afeta a função hepática, utilizando NPMs. Através de uma abordagem de aquisição de imagens em tempo real pelo sistema BAC, monitorou-se o perfil de distribuição das NPMs após a administração intravenosa. Para avaliar o perfil da biodistribuição, regiões de interesse (ROIs) foram selecionadas em partes referentes ao fígado e ao coração nas imagens de acordo com as referências anatômicas. Os sinais obtidos permitiram empregar um protocolo da quantificação de parâmetros farmacocinéticos, que indicaram que captação hepática é realmente comprometida durante a cirrose, o que influencia principalmente a troca de sangue entre o parênquima hepático e circulação. Uma vez que as células de Kupffer se mantiveram constantes durante a etapa cirrótica, o processo de capilarização dos sinusoide hepáticos foi considerado como a principal razão para a alteração da função hepática.

Palavras-chave: Biosuceptometria AC, Nanoparticulas magnéticas, Fígado, Nanotecnologia

ABSTRACT

This doctoral thesis includes the results of evaluations that were carried out in studies involving the Alternate Current Biosusceptometry system (ABC) and magnetic nanoparticles (MNPs). From a sequence of works using MNPs, the results presented here are essential steps for compressing physiological parameters of the biological system and pharmacokinetic parameters for MNPs. Both works addressed an assessment approach towards the liver, considered the main organ responsible for capturing NPMs from the bloodstream. The first work aimed to evaluate the biodistribution and clearance of MNPs profiles through long-time in vivo analysis and determine the elimination time carried out by the association between the ACB system and $MnFe_2O_4$ nanoparticles. In this study, it was possible to notice a higher uptake by the liver and the spleen due to their characteristics of retention and uptake. In 60 days, we observed an absence of MNPs in the spleen and a significant decay in the liver. We also determined the MNPs' half-life through the liver and the spleen elimination. The data indicated a concentration decay profile over the 60 days, which suggests that, in addition to elimination via feces, there is an endogenous mechanism of metabolization or possible agglomeration of MNPs, resulting in loss of ACB signal intensity.

Since magnetic nanoparticles (MNPs) present the possibility of being used as multifunctional probes to diagnose and treat liver diseases in recent years, the second study aimed to assess how the condition of cirrhosis influences and affects liver function. Using a real-time image acquisition approach, the distribution profile of MNPs after intravenous administration was monitored. We assessed the biodistribution profile based on the ACB images obtained through regions of interest (ROIs) selected in the heart and liver position according to the anatomical references previously settled. The signals obtained allowed the quantification of pharmacokinetic parameters, indicating that hepatic uptake is compromised during cirrhosis, which mainly influences blood exchange between the liver parenchyma and circulation. Since Kupffer cells remained constant during the cirrhotic stage, capillarization of the hepatic sinusoids was considered the main reason for the change in liver function.

Keywords: AC Biosuceptometry, Magnetic Nanoparticles, Liver, Nanotechnology

Sumário

INTRODUÇÃO GERAL

INTRODUÇÃO E ESTADO DA ARTE

A nanotecnologia é uma área de pesquisa que visa entender as propriedades e aplicar estruturas com dimensão na escala de nanômetros [1]. Nos últimos anos, a nanotecnologia tem atraído grande interesse da comunidade científica devido às suas inúmeras possibilidades em diversas áreas da ciência, abrangendo desde aplicações na área de ciências básicas como química e física até áreas aplicadas como engenharias, biomedicina, medicina entre outras.

No início do século XX, Paul Ehrlich idealizou o conceito de um carreador ideal que transportaria fármacos eficientemente moléculas para locais específicos, como tumores. Esse carreador atuaria como uma "bala mágica", atingindo seletivamente um patógeno sem afetar o hospedeiro. [2, 3] Com o avanço da nanotecnologia, pode-se visualizar as nanoparticulas como as possiveis "balas mágicas".

Nanopartículas são objetos pequenos variando de 1 a 100 nm, e em sua composição pode conter uma grande quantidade de materiais. As nanopartículas magnéticas (NPMs) são uma classe de nanopartículas que atraem um interesse significativo e se destacam em áreas da saúde, principalmente em aplicações biomédicas. Alguns tipos de NPMs, compostas principalmente de óxido de ferro, já são utilizadas como agente de contraste em Imagiamento por Ressonância Magnética (MRI – do inglês *Magnetic Resonance Imaging*), se apresentando como uma interessante alternativa aos convencionais contrastes a base de gadolíneo [4]. Também já existem tratamentos que empregam o uso de NPMs no combate ao câncer, como é o caso da hipertermia magnética [5] tratamento que consiste em guiar as NPMs ao tecido alvo (tumor) e aplicar um campo magnético de alta intensidade e com frequência específica, provocando o aquecimento das partículas e,

consequentemente, destruindo o tecido tumoral [6]. Além das aplicações citadas acima, ainda se destacam outras, como marcação, acompanhamento e ativação celular *in vitro* e *in vivo*, envolvendo diferentes tipos de células (dependendo do objetivo da aplicação), como por exemplo, células-tronco, macrófagos, entre outras. Devido a essa grande versatilidade e às propriedades intrínsecas das NPMs, elas também têm sido propostas como agentes teranósticos [7, 8], combinando ações terapêuticas e diagnósticas em uma mesma NPM.

A farmacocinética das NPMs é uma das principais preocupações quando estas são aplicadas em experimentos *in vivo* e procedimentos clínicos. Características como: carga superficial, diâmetro e revestimento das NPMs possibilitam diferentes alvos e destinos em um organismo. Esses parâmetros conferem às NPMs características de afinidade ou repulsão a certos tecidos, órgãos ou sistemas, o que faz com que estudos de caracterização pré-clínica, que tem como objetivo elucidar as relações entre a estrutura e a atividade das NPMs dentro de um organismo, sejam de grande importância na área [9-11].

Além das características das NPMs, outro fator de importância na farmacocinética das NPMs são as características morfológicas e fisiológicas dos órgãos, sendo que essas características estão intimamente ligadas às suas funções. A relação entre as características dos órgãos e as características das NPMs é alvo de vários estudos. Por exemplo, nanopartículas maiores do que 200 nm são sequestradas por filtração no baço [12], enquanto que nanopartículas menores do que 6 nm são rapidamente retiradas do sangue via depuração renal [9, 13]. Dessa forma, NPMs com diâmetros entre 6 e 200 nm têm como seu principal destino final o sistema retículo endotelial, apresentando maiores acúmulos no fígado [9, 14, 15].

A captação destas NPMs no fígado tem sido amplamente estudada nas últimas décadas, e se apresentaram como uma boa opção para a realização de marcação hepática em procedimentos MRI[16].

Estudos pré-clínicos são fundamentais para elucidar paramentos fisiológicos e farmacocinéticos a fim de atingir o real potencial translacional das NPMs. Para isso, as NPMs quando administradas devem ser detectadas *in vivo* e em tempo real. Adicionalmente, é necessário avaliar suas possíveis interações biológicas e perfis de biodistribuição, retenção, eliminação. Em comparação a outras nanopartículas, as NPMs são preferencialmente escolhidas na área médica devido às suas características de toxicidade mínima e excelentes propriedades físico-químicas. [17, 18] Contudo, mesmo sob essa perspectiva, os efeitos em longo prazo da agregação e depósito das NPMs depositados no fígado e baço ainda são desconhecidos. Ao longo dos anos, algumas NPMs como Feridex® (Bayer Healthcare), Resovist® (Bayer Healthcare), Combidex®(AMAG Pharma), Sinerem® (Guerbet), Clariscan® (Nycomed), and VSOP C184 (Ferropharm) foram aprovadas pelo FDA (do inglês- *Food and Drug Administration)* como agentes de contraste direcionados a exames de MRI. No entanto, todas as formulações foram descontinuadas do mercado devido a eficazes ou preocupações de segurança. [19-21] À visto disso, a fim de garantir o futuro da segurança em aplicações *in vivo*, ainda é interessante avaliar a biodistribuição e a liberação dependente do tempo da NPMs.

Ao longo dos anos, o sistema de biosusceptometria de corrente alternada (BAC) foi utilizado em inúmeros estudos direcionados à avaliação de parâmetros fisiológicos e farmacocinéticos, seja através de modelo animal ou até mesmo em humanos.

O sistema se enquadra na área de biomagnetismo, estudando campos magnéticos provenientes do sistema biológico. Alguns trabalhos em biomagnetismo como magnetoencefalografia, magnetocardiografia e magnetogastrografia tem o enfoque em avaliar pequenos campos, provenientes de correntes biológicas.[22-26] Outros estudos biomagnéticos são realizados monitorando traçadores ou marcadores que se encontram distribuídos em órgãos e tecidos. [27-29] Dessa forma, o sistema BAC inclui estudos direcionados a avaliar traçadores em sistemas biológicos. Através de um arranjo de bobinas, o sistema se comporta como um detector de material magnético que pode sem empregado em avaliações *in vitro* e *in vivo*.

Inicialmente, o sistema era exclusivamente dedicado a estudos relacionados a avaliações de parâmetros fisiológicos e biofísicos do sistema digestório. Após os primeiros trabalhos serem reportados na década de 70, foi na década de 90 que a instrumentação do sistema foi eficientemente aperfeiçoada por Miranda e colaboradores [30], no qual foi apresentado um arranjo um duplo transformador de fluxo, constituído por dois pares de bobinas (excitação e detecção). O par mais distante do material magnético atua como referência. Cada par de bobinas é separado por uma distância suficiente para minimizar a interferência entre elas (linhas de base), estando as bobinas detectoras dispostas em uma configuração gradiométrica de primeira ordem, ou seja, dispostas em sentidos contrários de modo que os fluxos magnéticos concatenados em cada bobina detectora sejam subtraídos. Essa conformação geométrica atua, então, eliminando os ruídos ambientais e tornando o sistema mais sensível. As bobinas excitadoras induzem fluxos magnéticos iguais nas bobinas detectoras, e ao aproximar um material com alta susceptibilidade magnética próximo da bobina detectora, há um desbalanceamento do fluxo magnético total do sistema, e observa-se um aumento no sinal elétrico obtido. Esse sinal elétrico pode ser medido, digitalizado e registrado online com

o auxílio de um amplificador sensível à fase (*Lock-in*), uma placa analógico/digital e um computador.

A partir disso, a nova configuração se apresentou mais sensível, necessitando de menos material magnético para realizar a detecção. [29] Com os seguintes aperfeiçoamentos, Moreira *et.al.*(2000) empregaram o sistema numa abordagem de mapeamento e obteve as primeiras imagens biomagnéticas *in vitro*. Diferentemente ao arranjo Monocanal BAC (BAC-Mono) que apresentava apenas uma bobina de detecção, um arranjo com número maior de bobinas de detecção foi proposto, a fim de avaliar dinamicamente processos biológicos.

O sistema Multicanal BAC (BAC-MC), caracterizado por apresentar sete bobinas de detecção, permite uma aquisição simultânea da distribuição de um determinado material magnético. Devido a nova configuração e não havendo necessidade de varredura, o sistema foi empregado em estudos direcionados a aquisições dinâmicas da distribuição de materiais magnéticos, de forma *in vitro* e *in vivo*. [27, 28, 31, 32] Além disso, o sistema tem como principal característica a alta resolução temporal, o que permite adquirir sinais que são convertidos em matrizes temporais, que quando processadas podem ser representadas por imagens.[33]

Após anos dedicados em registrar a motilidade gastrointestinal através da utilização de micropartículas de ferrita de manganês, Quini *et.al.* investigaram parâmetros do trânsito gastrointestinal através de uma abordagem em tempo real, reportando pela primeira vez a associação entre o sistema BAC como detector e as NPMs como traçador.[34] Consequentemente, o sistema BAC-Mono foi aplicado para detectar NPMs e compreender funções de diversos órgãos e tecidos.[35-39]

Paralelamente, o sistema BAC-MC foi aperfeiçoado para detecção e monitoramento de NPMs, no qual recentemente desenvolveu-se uma nova configuração aumentando o diâmetro das bobinas de excitação e bobinas detectoras. Outrora, Cora *et.al.* desenvolveu e aplicou um arranjo Multicanal constituído por um par de bobinas de excitação (com raio de 11 cm) e sete pares de bobinas de detecção (com raio de 2 cm), distribuídas circularmente dentro da bobina de excitação, para detectar no estômago humano o processo de desintegração de comprimidos marcados magneticamente, usando pó de ferrita de manganês. [27, 28, 40] Neste último caso, o sistema foi otimizado para detectar grandes quantidades de material magnético (1,0 g de pó de ferrita em um comprimido de 10 mm). Para adquirir de forma dinâmica sinais da distribuição de NPMs no sistema biológico de animais, desenvolveu-se um novo sistema BAC-MC composto por um par de bobinas de excitação (com raio de 10,5 cm) e dez pares de bobinas de detecção (com raio de 1 cm) distribuídas em configuração elíptica, o que asseguraria que toda a região torácica e abdominal do animal fosse coberta.

Como resultado desses aperfeiçoamentos realizados no sistema BAC-MC, foi possível pela primeira vez, adquirir imagens magnéticas em tempo real da chegada e saída das NPMs no coração do animal (após administração endovenosa) e sua subsequente chegada e retenção no fígado do animal. Além disso, a partir do estudo da intensidade de sinal ao longo do tempo em Regiões de Interesse (ROIs) (fígado e coração), foi possível estabelecer um modelo matemático que compreendesse a relação de transferência das NPMs da circulação sanguínea para o fígado. [41]

Apesar das seguintes utilizações do sistema BAC para novos estudos que incluíram avaliações *in vivo* de perfusão renal, perfusão cerebral, lesões renais, esvaziamento gástrico, captação hepática, tempo de circulação, além de biodistribuição e internalização celular das NPMs em situação *in vitro* e *ex vivo*, o sistema ainda demandava por

ferramentas computacionais e metodológicas a fim de oferecer reconstruções quantitativas da distribuição espacial de NPMs. Nesse contexto, o sistema BAC foi aprimorado fim de a se oferecer a possibilidade de aquisição de imagens quantitativas em tempo real. Dessa forma, a partir de um estudo recentemente publicado criou e implementou-se modelos matemáticos e computacionais para a resolução do problema inverso dos sistemas BAC, o que permitiu que o sistema ofereça imagens quantitativas de distribuição de NPMs.[42]

Mesmo com todo apelo da utilização das NPMs ao considerar todas as vantagens que possuem, as técnicas que atualmente são dedicadas a detecção NPMs de forma direta, ou seja, por meio de suas características magnéticas, apresentam certas limitações. Sistemas como MRI, o sistema de Imagiamento de Partículas Magnéticas (MPI – do inglês *Magnetic Particle Imaging*) e os Dispositivos Supercondutores de Interferência Quântica (SQUID- do inglês *Superconducting Quantum Interference Device*) [43-45] além de oferecerem a possibilidade de imagens ainda apresentam boa resolução espacial como principal vantagem, porem compartilham limitações como alta complexidade, limitações no campo de visão (FOV), necessidade de ambiente magneticamente blindado, alto custo do equipamento e manutenção.

Devido às numerosas vantagens que possui a utilização do sistema BAC em ambientes laboratoriais se torna adequada para a detecção de NPMs. Contrariamente a outros sistemas anteriormente citados, o sistema não faz uso de radiação ionizante e não necessita de blindagem magnética para aquisição de sinais. Dessa forma, o sistema apresenta excelente versatilidade além de baixo custo, uma vez que o arranjo é facilmente desenvolvido de forma simples.

Tratando-se do tecido hepático, a cirrose hepática tem despertado a atenção governamental e científica.[46] A cirrose hepática é uma doença que atinge o fígado, como consequência de lesões repetitivas não tratadas em um longo período, geradas por consumo crônico de álcool, doenças como hepatite C, entre outros. Caracteriza-se a cirrose o estado fibrótico disseminado, surgimentos de nódulos no tecido e também o surgimento de micro fístulas entre vasos aferentes e eferentes, determinando a não reversibilidade das lesões.[47, 48] Atualmente, é discutido que um número significativo de pessoas desenvolverá cirrose hepática devido à falta de atenção médica, considerando que a cirrose é uma etapa das hepatopatias crônicas, que muitas vezes evolui para o carcinoma hepatocelular. De acordo com a literatura, a cirrose juntamente com outras doenças hepáticas crônicas é responsável por mais de 2 milhões de mortes anuais em todo o mundo.[49]

Em relação ao tratamento de doenças hepáticas, várias abordagens convencionais têm sido empregadas principalmente para suprimir a inflamação hepática usando drogas antifibróticas. No entanto, a maioria dessas terapias não é eficaz provavelmente devido ao fato de a liberação do fármaco não ser específica, uma vez que vários tipos de células hepáticas são responsáveis pela inflamação hepática. [50-52] Desta forma, a dificuldade de entregar dose suficiente de agentes farmacológicos ao fígado, e o fato da não especificidade do direcionamento à estruturas celulares, a perspectiva de tratamento de doenças hepáticas continua sendo um desafio.

A partir do desenvolvimento da nanotecnologia, as NPMs têm chamado a atenção devido à possibilidade de serem usadas como sondas multifuncionais para diagnóstico e tratamento voltados a doenças hepáticas [53-57], apresentando-se se como uma ferramenta alternativa as estratégias convencionais.[58-60]

O atual documento a ser apresentado contempla resultados significativos dos estudos empregando a técnica de Biosusceptmetria AC para avaliações biológicas e funcionais. Os estudos foram realizados no Laboratório de Biomagnetismo (BIOMAG) do Instituto de Biociências de Botucatu sob coordenação do Prof. Titular Jose Ricardo de Arruda Miranda.

O grupo vem utilizando NPMs de ferrita de manganês recobertas com citrato (Cit-$MnFe_2O_4$) que se mostraram adequadas ao sistema BAC, uma vez que essas ferritas podem ser consideradas "macias" e apresentam sua excelente resposta magnética de baixo campo. Além disso, as NPMs de $MnFe_2O_4$ possuem alta saturação de magnetização que, em associação com o sistema BAC em sua função trabalho (2mT e frequência de 10 kHz) demonstram alta suscetibilidade magnética e consequentemente uma boa detecção para o sistema. Além disso, as NPMs de Cit-$MnFe_2O_4$ apresentam propriedades interessantes à hipertermia magnética, como demonstrado pelo grupo do Prof. Dr. Andris Bakuzis da Universidade Federal de Goiás (UFG).[61, 62]

Desde que se iniciaram os estudos utilizando as NPMs como traçadores magnéticos, o grupo vem dedicando uma série de trabalhos, em que foi possível desenvolver protocolos para avaliar processos farmacocinéticos das NPMs sob inúmeras circunstancias. Foram avaliados e investigados os perfis de distribuição, acúmulo e *clearance* das NPMs, o que permitiu inferir sobre a fisiologia de órgãos e sistemas em condições saudáveis e sob disfunções.

Adicionalmente, o sistema foi aprimorado a fim de reconstruir quantitativamente a distribuição 2D de NPMs, o que marcou substancialmente a linha de pesquisa do grupo, e contribuiu para alcançar resultados expressivos através de publicações mais sólidas e

consistente, já que anteriormente o grupo realizava o mapeamento das NPMs representados através de imagens não quantitativas.

Desde seus estudos iniciais envolvendo NPMs, o fígado sempre despertou a atenção do aluno que disserta esse documento. Alvo de seus estudos, durante o mestrado o aluno investigou o a captação hepática de NPMs e modelou as constantes de troca entre a corrente sanguínea. E pela reportou pela primeira vez a possibilidade de realizar o monitoramento de NPMs em tempo real através de imagens.

O atual documento abrange dois capítulos que serão apresentados artigos científicos envolvendo avaliações de biodistribuição e eliminação de NPMs utilizando o sistema BAC como detector.

O Capítulo II contempla a investigação a distribuição e eliminação de NPMs em tempos longos, avaliando a biodistribuição e depuração de perfis de NPMs através de análises de longo tempo, a fim de determinar o tempo de eliminação. O trabalho teve como principal foco o fígado, avaliando parâmetros farmacocinéticos do tecido hepático frente ao deposito de NPMs até 60 dias.

O Capítulo III é referente à análise da função hepática em condição de cirrose hepática induzida, avaliada através da utilização de NPMs e o sistema BAC. Assim como no mestrado do aluno, nesse trabalho é reportada a aquisição dinâmica da distribuição de NPMs em tempo real através de imagens magnéticas. Diferentemente do trabalho publicado durante mestrado, é apresentado um avanço significativo obtido durante o doutorado do aluno. Pela primeira vez foi possível reconstruir quantitativamente a distribuição das NPMs, o que permitiu alcançar resultados mais expressivos e robustos.

Referencias Bibliográficas

1. Ferrari, M., *Cancer nanotechnology: opportunities and challenges.* Nat Rev Cancer, 2005. **5**(3): p. 161-71.

2. Rodallec, A., et al., *Pharmacokinetics variability: Why nanoparticles are not just magic-bullets in oncology.* Critical Reviews in Oncology/Hematology, 2018. **129**: p. 1-12.
3. Granucci, F. and D. Prosperi, *Nanoparticles: "magic bullets" for targeting the immune system.* Semin Immunol, 2017. **34**: p. 1-2.

4. Gale, E.M., et al., *A Manganese Alternative to Gadolinium for MRI Contrast.* J Am Chem Soc, 2015. **137**(49): p. 15548-57.

5. Giustini, A.J., et al., *Magnetic Nanoparticle Hyperthermia in Cancer Treatment.* Nano Life, 2010. **1**(1n02).

6. Kumar, C.S. and F. Mohammad, *Magnetic nanomaterials for hyperthermia-based therapy and controlled drug delivery.* Adv Drug Deliv Rev, 2011. **63**(9): p. 789-808.

7. Shubayev, V.I., T.R. Pisanic, 2nd, and S. Jin, *Magnetic nanoparticles for theragnostics.* Adv Drug Deliv Rev, 2009. **61**(6): p. 467-77.

8. Frimpong, R.A. and J.Z. Hilt, *Magnetic nanoparticles in biomedicine: synthesis, functionalization and applications.* Nanomedicine (Lond), 2010. **5**(9): p. 1401-14.

9. Sun, C., J.S. Lee, and M. Zhang, *Magnetic nanoparticles in MR imaging and drug delivery.* Adv Drug Deliv Rev, 2008. **60**(11): p. 1252-65.

10. Lubbe, A.S., et al., *Preclinical experiences with magnetic drug targeting: tolerance and efficacy.* Cancer Res, 1996. **56**(20): p. 4694-701.

11. Albanese, A., P.S. Tang, and W.C. Chan, *The effect of nanoparticle size, shape, and surface chemistry on biological systems.* Annu Rev Biomed Eng, 2012. **14**: p. 1-16.

12. Chen, L.T. and L. Weiss, *The role of the sinus wall in the passage of erythrocytes through the spleen.* Blood, 1973. **41**(4): p. 529-37.

13. Choi, H.S., et al., *Renal clearance of quantum dots.* Nature Biotechnology, 2007. **25**(10): p. 1165-70.

14. Ruoslahti, E., S.N. Bhatia, and M.J. Sailor, *Targeting of drugs and nanoparticles to tumors.* Journal of Cell Biology, 2010. **188**(6): p. 759-768.

15. Gamarra, L.F., et al., *Ferromagnetic resonance for the quantification of superparamagnetic iron oxide nanoparticles in biological materials.* Int J Nanomedicine, 2010. **5**: p. 203-11.

16. Reimer, P. and T. Balzer, *Ferucarbotran (Resovist): a new clinically approved RES-specific contrast agent for contrast-enhanced MRI of the liver: properties, clinical development, and applications.* Eur Radiol, 2003. **13**(6): p. 1266-76.

17. Malhotra, N., et al., *Potential Toxicity of Iron Oxide Magnetic Nanoparticles: A Review.* Molecules (Basel, Switzerland), 2020. **25**(14): p. 3159.

18. Coricovac, D.-E., et al., *Biocompatible colloidal suspensions based on magnetic iron oxide nanoparticles: synthesis, characterization and toxicological profile.* 2017. **8**: p. 154.

19. Stueber, D.D., et al., *Magnetic nanoparticles in biology and medicine: Past, present, and future trends.* 2021. **13**(7): p. 943.

20. Wahsner, J., et al., *Chemistry of MRI contrast agents: current challenges and new frontiers.* 2018. **119**(2): p. 957-1057.

21. Anselmo, A.C., S.J.B. Mitragotri, and t. medicine, *Nanoparticles in the clinic: An update.* 2019. **4**(3): p. e10143.

22. Maestu, F., et al., *Evidence of biochemical and biomagnetic interactions in Alzheimer's disease: an MEG and MR spectroscopy study.* 2005. **20**(2-3): p. 145-152.

23. Mooney, J.W., *A Biomagnetic Field Mapping System for Detection of Heart Disease in a Clinical Environment*. 2018, University of Leeds.

24. la Roca-Chiapas, J.M.D. and T. Cordova-Fraga, *Biomagnetic techniques for evaluating gastric emptying, peristaltic contraction and transit time.* World journal of gastrointestinal pathophysiology, 2011. **2**(5): p. 65-71.

25. Somarajan, S., et al., *Noninvasive magnetogastrography detects erythromycin-induced effects on the gastric slow wave.* 2018. **66**(2): p. 327-334.

26. Ueno, S. and M. Sekino, *Biomagnetics: principles and applications of biomagnetic stimulation and imaging*. 2018: CRC Press.

27. Cora, A., et al., *Magnetic images of the disintegration process of tablets in the human stomach by ac biosusceptometry.* Phys Med Biol, 2005. **50**.

28. Cora, L.A., et al., *Disintegration of magnetic tablets in human stomach evaluated by alternate current biosusceptometry.* Eur J Pharm Biopharm, 2003. **56**(3): p. 413-20.

29. Baffa, O., et al., *Analysis and development of AC biosusceptometer for orocaecal transit time measurements.* Med Biol Eng Comput, 1995. **33**(3): p. 353-7.

30. Miranda, J.R., et al., *An AC biosusceptometer to study gastric emptying.* Med Phys, 1992. **19**(2): p. 445-8.

31. Pinto, L.A., et al., *Pharmacomagnetography to evaluate the performance of magnetic enteric-coated tablets in the human gastrointestinal tract.* European Journal of Pharmaceutics and Biopharmaceutics, 2021. **161**: p. 50-55.

32. Corá, L.A., et al., *Pharmaceutical applications of AC Biosusceptometry.* European journal of pharmaceutics and biopharmaceutics, 2010. **74**(1): p. 67-77.

33. Soares, G.A., et al., *The Influence of Omeprazole on the Dissolution Processes of pH-Dependent Magnetic Tablets Assessed by Pharmacomagnetography.* 2021. **13**(8): p. 1274.

34. Quini, C.C., et al., *Employment of a noninvasive magnetic method for evaluation of gastrointestinal transit in rats.* J Biol Eng, 2012. **6**(1): p. 6.

35. Próspero, A.G., et al., *Dynamic cerebral perfusion parameters and magnetic nanoparticle accumulation assessed by AC biosusceptometry.* Biomed Tech (Berl), 2020. **65**(3): p. 343-351.

36. Quini, C.C., et al., *Development of a protocol to assess cell internalization and tissue uptake of magnetic nanoparticles by AC Biosusceptometry.* Journal of Magnetism and Magnetic Materials, 2019. **473**: p. 527-533.

37. Próspero, A.G., et al., *Real-time in vivo monitoring of magnetic nanoparticles in the bloodstream by AC biosusceptometry.* Journal of nanobiotechnology, 2017. **15**(1): p. 1-12.

38. Quini, C.C., et al., *Real-time liver uptake and biodistribution of magnetic nanoparticles determined by AC biosusceptometry.* Nanomedicine, 2017. **13**(4): p. 1519-1529.

39. Quini, C.C., et al., *Renal perfusion evaluation by alternating current biosusceptometry of magnetic nanoparticles.* Journal of Magnetism and Magnetic Materials, 2015. **380**: p. 2-6.

40. Corá, L.A., et al., *Enteric coated magnetic HPMC capsules evaluated in human gastrointestinal tract by AC biosusceptometry.* 2006. **23**(8): p. 1809-1816.

41. Soares, G., et al., *Multichannel AC Biosusceptometry system to map biodistribution and assess the pharmacokinetic profile of magnetic nanoparticles by imaging.* IEEE Trans Nanobioscience, 2019.

42. Biasotti, G.G.d.A., et al., *2D Quantitative Imaging of Magnetic Nanoparticles by an AC Biosusceptometry Based Scanning Approach and Inverse Problem.* Sensors, 2021. **21**(21): p. 7063.

43. Liebl, M., et al., *Magnetorelaxometry procedures for quantitative imaging and characterization of magnetic nanoparticles in biomedical applications.* Biomed Tech (Berl), 2015. **60**(5): p. 427-43.

44. Weizenecker, J., et al., *Three-dimensional real-time in vivo magnetic particle imaging.* Phys Med Biol, 2009. **54**(5): p. L1-L10.

45. Ellis, C.M., J. Pellico, and J.J.J.M. Davis, *Magnetic nanoparticles supporting bio-responsive T1/T2 magnetic resonance imaging.* 2019. **12**(24): p. 4096.

46. Levada, K., et al., *Magnetic-assisted treatment of liver fibrosis.* Cells, 2019. **8**(10): p. 1279.

47. Li, J. and B. Tuo, *Current and Emerging Approaches for Hepatic Fibrosis Treatment.* Gastroenterology research and practice, 2021. **2021**: p. 6612892-6612892.

48. Sun, T., et al., *Nanomaterials and hepatic disease: toxicokinetics, disease types, intrinsic mechanisms, liver susceptibility, and influencing factors.* Journal of Nanobiotechnology, 2021. **19**(1): p. 108.

49. Moon, A.M., A.G. Singal, and E.B. Tapper, *Contemporary Epidemiology of Chronic Liver Disease and Cirrhosis.* Clin Gastroenterol Hepatol, 2020. **18**(12): p. 2650-2666.

50. Ezhilarasan, D.J.E.J.o.P., *Advantages and challenges in nanomedicines for chronic liver diseases: A hepatologist's perspectives.* 2021. **893**: p. 173832.

51. Bai, X., G. Su, and S. Zhai, *Recent Advances in Nanomedicine for the Diagnosis and Therapy of Liver Fibrosis.* Nanomaterials, 2020. **10**(10): p. 1945.

52. Jin, Y., et al., *Applications of Nanobiomaterials in the Therapy and Imaging of Acute Liver Failure.* Nano-Micro Letters, 2020. **13**(1): p. 25.

53. Ahlawat, J., et al., *Nanoparticles in Biomedical Applications*, in *Green Nanoparticles*. 2020, Springer, Cham. p. 227-250.

54. Talaei, S., et al., *17-Allylamino-17-demethoxygeldanamycin loaded PCL/PEG nanofibrous scaffold for effective growth inhibition of T47D breast cancer cells.* Journal of Drug Delivery Science and Technology, 2019. **49**: p. 162-168.

55. Yu, Z., et al., *Nanoparticles: A New Approach to Upgrade Cancer Diagnosis and Treatment.* Nanoscale Research Letters, 2021. **16**(1): p. 88.

56. Yao, Y., et al., *Nanoparticle-Based Drug Delivery in Cancer Therapy and Its Role in Overcoming Drug Resistance.* Frontiers in Molecular Biosciences, 2020. **7**(193).

57. Patra, J.K., et al., *Nano based drug delivery systems: recent developments and future prospects.* Journal of Nanobiotechnology, 2018. **16**(1): p. 71.

58. Li, Y., et al., *The diagnosis of hepatic fibrosis by magnetic resonance and near-infrared imaging using dual-modality nanoparticles.* RSC advances, 2018. **8**(12): p. 6699-6708.

59. Saraswathy, A., et al., *Asialoglycoprotein receptor targeted optical and magnetic resonance imaging and therapy of liver fibrosis using pullulan stabilized multi-functional iron oxide nanoprobe.* Scientific Reports, 2021. **11**(1): p. 18324.

60. Nagórniewicz, B., et al., *Engineered Relaxin as theranostic nanomedicine to diagnose and ameliorate liver cirrhosis.* Nanomedicine: Nanotechnology, Biology and Medicine, 2019. **17**: p. 106-118.

61. Bakuzis, A. and P. Morais, *On the origin of the surface magnetic anisotropy in manganese–ferrite nanoparticles.* Journal of magnetism and magnetic materials, 2001. **226**: p. 1924-1926.

62. Bakuzis, A.F., et al., *Chain formation and aging process in biocompatible polydisperse ferrofluids: experimental investigation and Monte Carlo simulations.* Adv Colloid Interface Sci, 2013. **191-192**: p. 1-21.

CAPÍTULO II

Long-Term Clearance and Biodistribution of Magnetic Nanoparticles Assessed by AC Biosusceptometry

materials

MDPI

Article

Long-Term Clearance and Biodistribution of Magnetic Nanoparticles Assessed by AC Biosusceptometry

Guilherme A. Soares [1,*], João V. C. Faria [1], Leonardo A. Pinto [1], Andre G. Prospero [1], Gabriele M. Pereira [1], Erick G. Stoppa [1], Lais P. Buranello [1], Andris F. Bakuzis [2], Oswaldo Baffa [3] and José R. A. Miranda [1]

[1] Department of Biophysics and Pharmacology, Institute of Biosciences, São Paulo State University—UNESP, Botucatu 18618-689, SP, Brazil; joao.faria@unesp.br (J.V.C.F.); leonardo.antonio@unesp.br (L.A.P.); andre.prospero@unesp.br (A.G.P.); gabriele.martinsp@gmail.com (G.M.P.); e.stoppa@unesp.br (E.G.S.); lais.buranello@unesp.br (L.P.B.); jose.r.miranda@unesp.br (J.R.A.M.)
[2] Institute of Physics, Federal University of Goiás, Goiânia 74690-900, GO, Brazil; abakuzis@gmail.com
[3] Faculty of Philosophy, Sciences and Letters at Ribeirão Preto, University of São Paulo, Ribeirão Preto 14040-900, SP, Brazil; baffa@usp.br
* Correspondence: guilherme.soares@unesp.br

Abstract: Once administered in an organism, the physiological parameters of magnetic nanoparticles (MNPs) must be addressed, as well as their possible interactions and retention and elimination profiles. Alternating current biosusceptometry (ACB) is a biomagnetic detection system used to detect and quantify MNPs. The aims of this study were to evaluate the biodistribution and clearance of MNPs profiles through long-time in vivo analysis and determine the elimination time carried out by the association between the ACB system and $MnFe_2O_4$ nanoparticles. The liver, lung, spleen, kidneys, and heart and a blood sample were collected for biodistribution analysis and, for elimination analysis, and over 60 days. During the period analyzed, the animal's feces were also collectedd. It was possible to notice a higher uptake by the liver and the spleen due to their characteristics of retention and uptake. In 60 days, we observed an absence of MNPs in the spleen and a significant decay in the liver. We also determined the MNPs' half-life through the liver and the spleen elimination. The data indicated a concentration decay profile over the 60 days, which suggests that, in addition to elimination via feces, there is an endogenous mechanism of metabolization or possible agglomeration of MNPs, resulting in loss of ACB signal intensity.

Keywords: magnetic nanoparticles; alternate current biosusceptometry; clearance; biodistribution; long-time analysis

Citation: Soares, G.A.; Faria, J.V.C.; Pinto, L.A.; Prospero, A.G.; Pereira, G.M.; Stoppa, E.G.; Buranello, L.P.; Bakuzis, A.F.; Baffa, O.; Miranda, J.R.A. Long-Term Clearance and Biodistribution of Magnetic Nanoparticles Assessed by AC Biosusceptometry. *Materials* **2022**, *15*, 2121. https://doi.org/10.3390/ma15062121

Academic Editors: Tatyana I. Shabatina and Olga I. Vernaya

Received: 19 November 2021
Accepted: 16 December 2021
Published: 14 March 2022

1. Introduction

Over the past few years, there has been increased use of magnetic nanoparticles (MNPs) in a range of biomedical applications, such as drug delivery, in vivo cell tracking, diagnostics, magnetic resonance imaging (MRI), and thermal ablation therapy [1–4]. Due to their advantages in several biomedical uses and the possibility to manipulate them according to their use, which improves the interactions with the biological systems, many studies have been developed to reach all MNP's benefits [5,6]. Besides understanding the MNPs composition and the surface functionality, it is necessary to comprehend the characterization of the MNPs in a biological system, which is essential to truly address the implications in future human medical applications. In addition, the real feasibility of these applications depends directly on the biodistribution and toxicity profiles [7].

The great challenge of nanomedicine is to offer multifunctional nanosystems biocompatible and non-toxic with biological targets [8,9]. Nowadays, the development, use, and study of the interactions of MNPs with biological systems have significantly increased, in contrast to the number of studies towards biodistribution, toxicity, and clearance studies. This divergence may be mainly attributed to the variety of MNPs used and to the methodologies applied.

Different routes may be used to infuse MNPs in the biological system, with the intravenous administration (IV) and intraperitoneal injection acting as the main routes [10]. IV injection remains the standard method to inject MNPs due to the instantaneous response provided and the possibility of obtaining much pharmacokinetic information. MNPs can be intravenously infused to be guided to a specific site such as a tumor, increasing treatment efficiency. Additionally, the IV route is useful for improving drug delivery efficacy, reducing the possible cytotoxicity of nanoparticles [11].

The size of the MNPs is a crucial factor for the biodistribution process. Consistent reports in the literature have demonstrated that MNPs larger than 100 nm in hydrodynamic diameter are primarily taken up by organs such as the liver, spleen, and lungs [12]. The main factor which contributes to this specific uptake is the mononuclear phagocytic system (MPS), also known classically as the reticuloendothelial system (RES), a complex network of cells specialized in the removal of xenobiotic materials from the bloodstream, broadly localized in these organs [13,14]. On the other hand, small MNPs (<10 nm) are virtually eliminated through renal clearance [15]. Moreover, the biodistribution is directly dependent on other physicochemical properties MNPs, including surface charge and coating [16,17].

Concerning the biodistribution of MNPs by these organs, well-established specialized tissue-resident macrophages are the main cells responsible for the uptake of nanoparticles. In general, MNPs preferentially accumulate in the liver and spleen, which are responsible for the sequestration of more than 95% of the nanoparticles due to the phagocytosis performed by the Kupffer cells the macrophages of the splenic marginal zone, respectively [18–20]. The liver is a highly perfused organ and extremely important in the uptake of both endogenous and exogenous substances due to its high blood flow, presenting liver sinusoidal endothelial cells (LSEC), which are highly fenestrated. The liver still has Kupffer cells and the resident localized macrophages, responsible for the uptake and elimination of many materials from the bloodstream [21]. Several studies have reported the intensive MNPs uptake carried by the hepatic structures, inclusive of the MNPs used in this work [22–25]. The spleen has a very interesting microanatomy, which can act as an efficient sieve to filter any exogenous material. The spleen is highly permeable vasculature with endothelial fenestrations. Moreover, the splenic vasculature is arranged as a way to facilitate the contact of MNPs and macrophages. The splenic arteries enter the organ and are finished off in highly porous capillaries, making the blood reach the marginal and red pulp zones [26]. These zones are the central splenic region for the MNPs uptake due to macrophages that phagocytize the MNPs. Studies reported the phagocytize process in the splenic zones through histological assessments or different biodistribution assessments methods [27]. Immediately after the injection, the MNPs are subjected to the opsonization process, characterized by the adsorption of plasma proteins on MNPs surface, allowing them to be easily recognized by the macrophages. As a result, this array of protein around the MNPs surface, often known as protein corona, increases the hydrodynamic size of MNPs; they are significantly removed from the bloodstream [28,29]. Physicochemical characteristics of MNPs may strongly influence the composition and architecture of the protein corona. Surface modifications of the MNPs shell are commonly carried out to modify their performance with biological targets. Coating the MNP with organic or inorganic molecules is one of the strategies widely employed to avoid the interaction with biological compounds [30]. Recently, Prospero and coworkers related that the protein corona composition is strongly dependent on MNPs characteristics, mainly including the size, the coating, and the surface charge. Indeed, this arrangement of protein makes the MNPs recognizable as a new complex biological structure that determines their biodistribution and clearance [31].

To achieve the real translational MNPs potential (theranostic), once they are administered in an organism, they must be detected in vivo and real-time to assess physiological parameters [32]. Additionally, it is necessary to evaluate their possible interactions and retention and elimination profiles. Nowadays, concerns about toxicity, safety, biodistribution, and clearance have emerged due to several MNPs applications [8,33].

Although several MNP biodistribution studies have recently been published, the process of the uptake and consequent metabolization and degradation of MNPs by the MPS remains unknown by nanomedicine [34]. Some literature works reported that the long-term accumulation may be beneficial for imaging and therapeutic applications [35], acting as a T2 contrast enhancement agent in MRI, either as a tracer or marker of new imaging modalities such as magnetic particle imaging and ACB imaging [22]. However, extensive pre-clinical trials must be addressed for real and future clinical applications [32], once the long-term effects of the MNPs aggregation deposited in the liver and spleen are still unknown [13]. Additionally, it is considered that MNPs retention has side effects for periods up to 11 months in the organs [36,37].

Over the years, there have been 51 nano-based products available for the therapies and diagnostic approved by the Food and Drug Administration (FDA) or European Medicine Agency (EMA) [38]. Nine MNPs are currently used as imaging agents, iron deficiency in chronic kidney disease (CKD), and magnetic hyperthermia regarding the inorganic and metallic nanoparticles [38,39]. Initially, based on the clinical success tests, FDA approved several MNPs to be used as MRI contrast agents, such as Feridex® (Bayer Healthcare), Resovist® (Bayer Healthcare), Combidex® (AMAG Pharma), Sinerem® (Guerbet), Clariscan® (Nycomed), and VSOP C184 (Ferropharm). However, all the formulations have been discontinued from the market by the FDA due to efficacy or safety concerns [38–41].

The toxicity and the biodistribution analysis have become an issue of concern and require extensive investigation [42]. Currently, the approval of MNP as any nanomedicines and drugs is regulated by FDA. The completed process involves efficacy, safety, and toxicity studies. Nevertheless, the FDA regimentation and approval process, as for any other regulated drug, a complete knowledge about the mechanisms of the interactions MNP with the biological system is not required [43].

Over the years, different imaging, spectroscopy, and magnetometry techniques have been used to detect and quantify the biodistribution of MNPs in animals. In addition to techniques such as MRI and MPI [41,44–46]. Alternating current biosusceptometry (ACB) is a biomagnetic detection system used to detect and quantify MNPs, recently employed in several biomedical applications [22–24,31,47].

Therefore, in this work, the study aimed to evaluate the biodistribution and clearance of MNPs profiles through long time analysis and determine the elimination time carried out by the association between the ACB system and $MnFe_2O_4$ nanoparticles coated with citrate (Cit-$MnFe_2O_4$ MNPs).

2. Materials and Methods

2.1. ACB System

The ACB system is a magnetic detector and has been recently used in several studies involving MNPs. The ACB system theory is based on the mutual induction between two induction and pickup coils coaxially arranged in a first-order gradiometer. If a current oscillating sinusoidally is applied along with the indication coils, an alternate magnetic field is generated as $H = H_a \sin(\omega t)$, where H_a is the field amplitude and ω is the angular frequency. Then, the differential induced voltage ($\Phi_1 - \Phi_2$ from the primary and secondary pickup coils) is detected and expressed according to Faraday's law:

$$V_d = -NA\frac{d\Phi}{dt} \quad (1)$$

When a sample is positioned at the center of one of the pickup coils, the magnetic flux induced by a sample with magnetization $M(H)$ in a pickup coil with is:

$$\Phi = -\mu_0 NAM\frac{d}{dt}[(M + H_a) - H_a] \quad (2)$$

The magnetic flux can be rewritten as an ideal balanced detection coil system:

$$\Phi = -\mu_0 NAM \frac{d}{dt}[(M + H_a) - H_a] \quad (3)$$

From Equation (3), the final voltage detected results:

$$V_d = -\mu_0 NAM \frac{dM(t)}{dt} \quad (4)$$

In this way, the instrumental arrangement turns the system into a magnetic flux transformer. The coil pair (excitation/detection) furthest from the sample acts as a reference, while the closest to the magnetic material acts as detection.

The MNP biodistribution and elimination signals quantification were carried out using an ACB setup already reported by [23,47]. As demonstrated previously, the setup presents high sensitivity and accuracy for ex vivo analysis. Figure 1 presents the schematic diagram of the ACB setup used for MNP measurements.

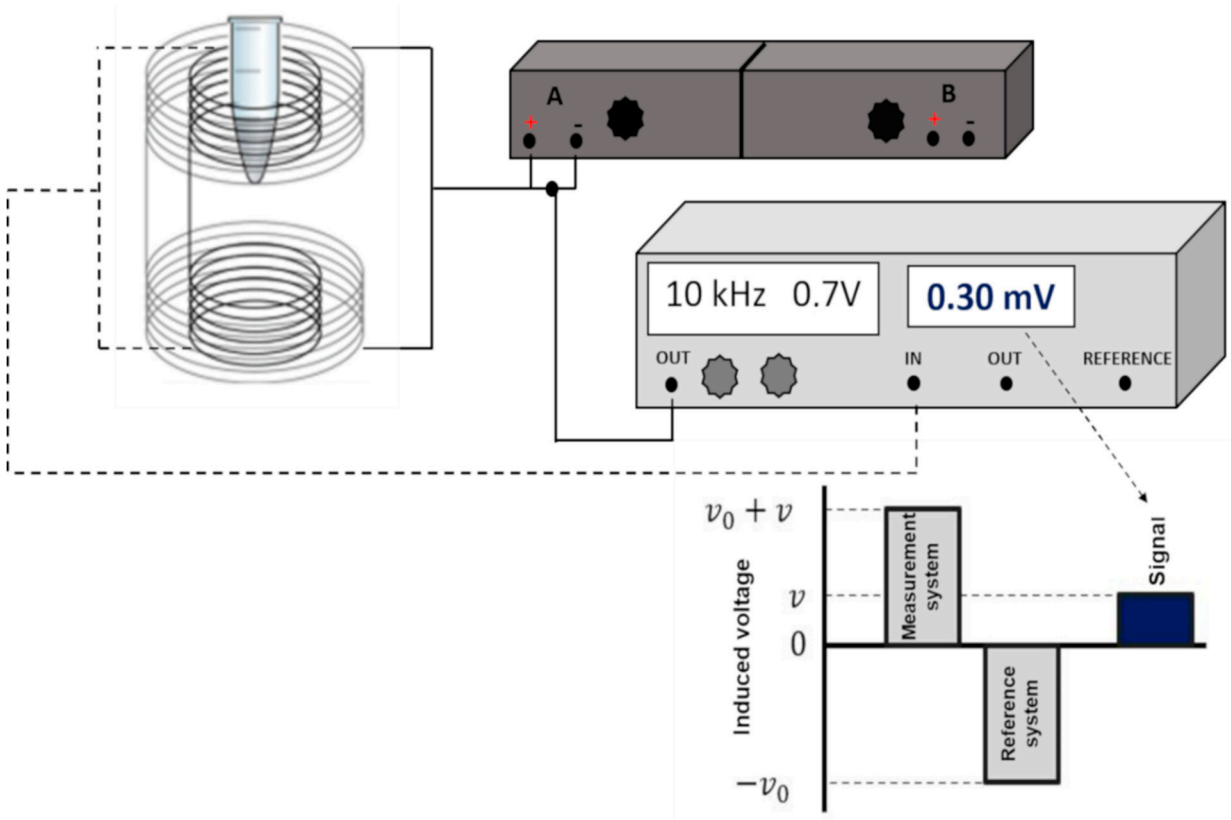

Figure 1. Schematic diagram of ACB setup used for MNP measurements. Through a phase-sensitive amplifier (lock-in—Stanford Research Systems SR830) (light grey), an electrical signal of 0.7 V at a frequency of 10 kHz is generated and is amplified by power amplifiers (−3 dB) (dark gray), in which the resulting current is applied to the excitation coils.

2.2. Magnetic Nanoparticles

We employed citrate-coated manganese ferrite (Ci-$MnFe_2O_4$), nanoparticles synthesized by a co-precipitation method previously characterized and described [31,47]. Ci-$MnFe_2O_4$ at a 23 mg/mL concentration presented a superparamagnetic behavior and a magnetization saturation of 264 kA/m. The MNPs characterization was performed by dynamic light scattering (DLS) Zetasizer NanoS (Malvern Instruments, Malvern, UK). and Transmission electron microscopy (TEM) (Jeol, Tokyo, Japan). All MNPs characterization can be found in the Supplementary material. Figure S1 shows the TEM images for the

magnetic nanoparticles, and Figure S2 shows the particles size distribution. Figure S3 presents the hydrodynamic distribution for the magnetic nanoparticles, Figure S4 presents the magnetization curve of the manganese-ferrite nanoparticles, and Figure S5 shows the X-ray diffraction pattern of the citrate-coated manganese-ferrite nanoparticles.

2.3. Animal Experiments

All animal experiments were previously approved and performed following the Committee on Ethics in Animal Use, under the protocol (CEUA)–IBB 1135.

Fifty male rats weighing 250–300 g (Rattus norvegicus albinus, Wistar; acquired from the Anilab, Paulinia, SP, Brazil) were subjected to ten groups that were established by the animal euthanasia time: 1 h, 4 h, 12 h, 24 h, 48 h, 5 days, 10 days, 15 days, 30 days, and 60 days.

All the animals were subjected to the same experimental protocol. The animals were anesthetized with isofluorane (5% for induction and 2% for maintenance) and underwent cannulation surgery of the left femoral vein for intravenous administration of MNPs. The animals received a single injection of 0.3 mL of MNPs (total of 6.9 mg of MNPs) at an administration rate of 0.03 mL/s and were euthanized by decapitation, referring to the time point.

To assess the biodistribution pattern as a function of time, the liver, lung, spleen, kidneys, and heart were collected. In addition, a sample of blood and feces was also collected. After the experimental procedure, all the collected samples were submitted to a Labconco FreeZone 2.5 benchtop freeze dryer (Labconco, Kansas City, MO, USA and stored in a volume-controlled flask.

2.4. Ex Vivo Biodistribution and Pharmacokinetic Assessment

The feces of the animals were collected every 24 h and were then subjected to the same freeze-drying process for further analysis to assess the MNPs elimination profile.

To provide an ex vivo quantitative evaluation about the MNP distribution previously in vivo administered, we also built a calibration curve for the two MNPs used here to compare the ACB signal obtained with ACB response to a known concentration of samples, owning a well-established mass of MNPs. To understand how MNP features and physiology can influence the liver MNP accumulation pattern, it was proposed to investigate the biodistribution data obtained from the ACB analysis through a pharmacokinetic model. Therefore, the MNP half-life in the bloodstream ($T_{1/2}$) can be modeled according to Equation (5):

$$Y_{(t)} = Y_0 + A_1 e^{-t/\tau 1} + e^{-t/\tau 2} \quad (5)$$

Equation (5) assumes that Y_0 corresponds to the ACB signal immediately before the injection, and $\tau 1$ and $\tau 2$ refer to the two average elimination exponential coefficients. At the same time, the parameters A_1 and A_2 (uptake indices), when summed, represent the total MNP accumulation at each instant. Regarding the spleen MNP clearance, its elimination was modeled using the following Equation (6):

$$Y_{(t)} = Y_0 + A_1 e^{-t/\tau 1} \quad (6)$$

Statistical calculations and half-life quantifications were performed using OriginLab 8.5 (Version 2016, OriginLab Corporation, Northampton, MA, USA).

3. Results

3.1. MNPs Characterization

Two methodologies were employed for the MNPs characterization. The hydrodynamic diameter was determined, followed by an analysis of ACB signal response to different concentrations of MNPs. Through the DLS analysis, MNPs hydrodynamic diameter and zeta potential were 40 ± 5.6 nm and -27.8 mV, respectively. The MNPs had a polydispersity

index of 0.175 ± 0.092. Figure 2 shows the calibration curve and the linear response of the ACB system for citrate-coated MNPs.

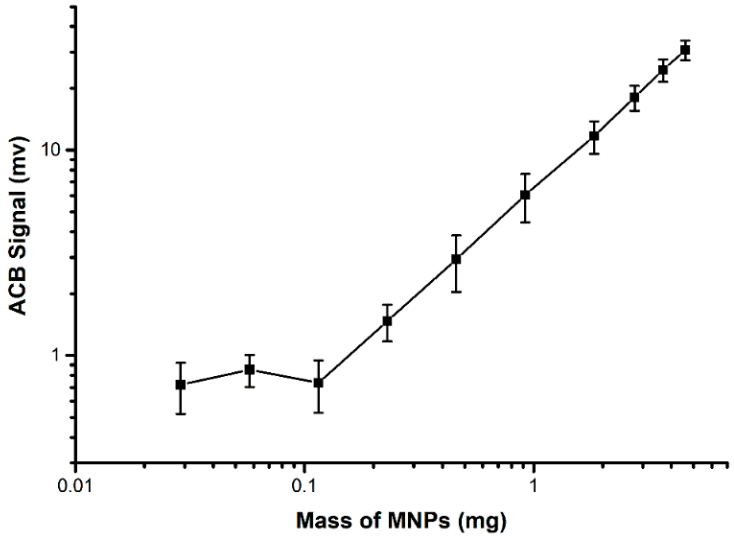

Figure 2. Calibration curve of citrate-coated MNPs in linear scale with linear fits, where an R^2 = 0.99 was obtained for citrate-coated MNPs.

3.2. MNPs Biodistribution and Elimination

Figure 3 shows the biodistribution of MNP Cit-$MnFe_2O_4$ in each organ, quantified from one hour until 60 days after the in vivo administration.

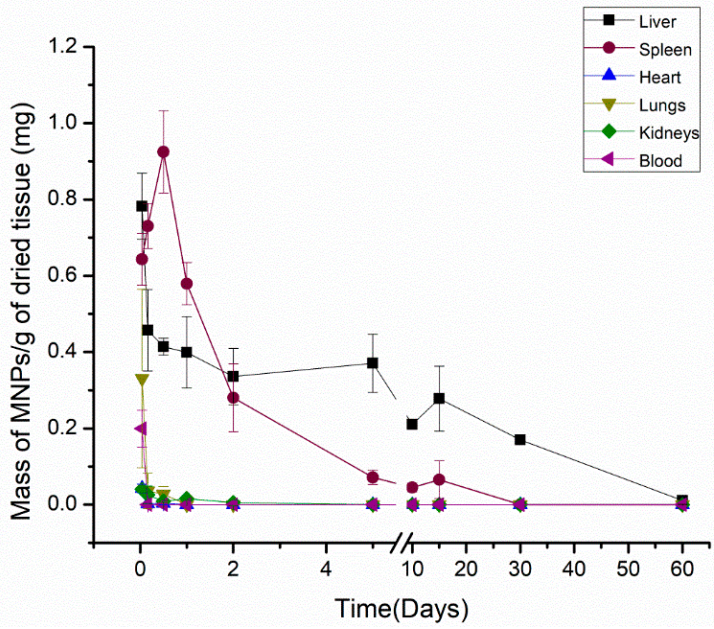

Figure 3. Biodistribution results for all organs of interest of the citrate-coated MNPs over the period evaluated.

As depicted in Figure 3, besides the predominant accumulation in the liver and spleen, MNPs were in all the organs from 1 h and until 12 h after the injection. In the liver, MPNs were detected along the entire measured period (60 days), presenting a maximum amount of MNP one hour after administration (5.4 mg of MNPs). At measurement times determined around 60 days, the amount of MNP reached low levels, around zero. MNPs were significantly detected within 15 days after in vivo administration regarding the spleen,

which presented the highest accumulation MNPs around 12 h (0.092 mg). Similar to the liver, the spleen MNPs signal tends to decrease with time, which can detect a very low mass of MNPs.

Despite the low ACB signal intensity, MNPs could be seen in the kidneys until 48 h. Both the heart and the lungs accumulated MNP for only 12 h, showing a maximum ACB signal of the MNP injection in one hour after the injection, which is the only time that it was possible to detect MNP circulating in the blood.

The data obtained through the quantification of the ABC system indicated that the elimination kinetics from the infusion of MNPs occur according to an exponential behavior. As the liver and spleen are considered the two main organs responsible for MNPs uptake from the bloodstream, the pharmacokinetics of the MNP pattern for both organs were compared, employing a bi-exponential model to determine the MNPs circulation half-life.

In a rat model, the Cit-$MnFe_2O_4$ exhibited biexponential liver concentration decay, with a half-life of 70 min for the initial phase, which is faster and responsible for the distribution and clearance for most of the injected dose. In contrast, the second phase is slower and presents a half-life of 30 days. Regarding the spleen half-life, a single-phase $T_{1/2}$ of 1.75 days was found. To quantify the amount of MNPs in the collected feces, we established a protocol to quantify the samples in five days (Figure 4)

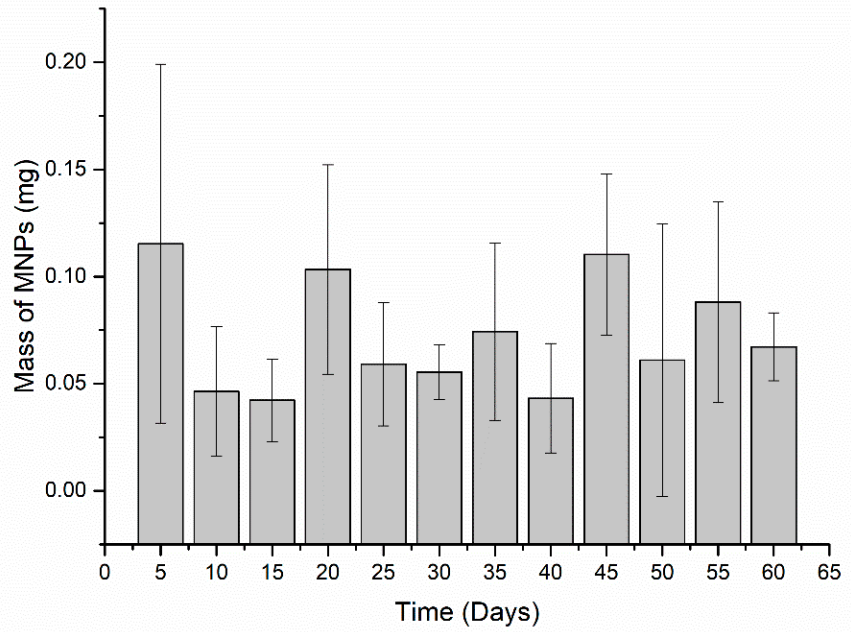

Figure 4. Elimination of MNPs via feces every five days. For statistical analysis, the Mann–Whitney U test was used. It was found no significant difference between the days ($p < 0.05$).

The highest elimination day occurred five days after administration, presenting 0.115 ± 0.08 mg MNPs eliminated. Although this initial period of five days showed the highest elimination values, no elimination pattern was noticed, considering that the values do not differ much from the other values found. Moreover, the elimination profile presents an approximate amount MNPs within 0.05 and 0.1 mg every five days. Additionally, the accumulated profile of MNPs elimination was assessed. Figure 5 shows the total of MNPs eliminated over the entire period.

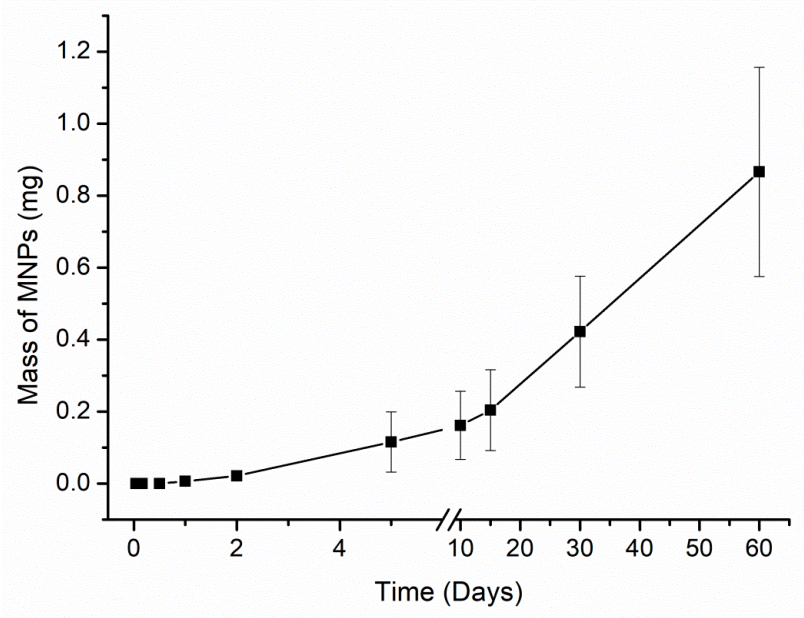

Figure 5. Cumulative elimination profile of Cit-$MnFe_2O_4$ MNPs via feces over the period evaluated.

Figure 5 indicates that the MNPs elimination precisely starts from two days after administration. It is worth pointing out that all animal feces were collected before euthanasia, and all feces were analyzed individually. The total clearance was 0.87 ± 0.29 mg MNPs.

4. Discussion

This study employed the ACB system to assess the biodistribution and elimination pattern via feces of Cit-$MnFe_2O_4$ MNPs over long periods after intravenous administration in rats. The soft-ferrite based MNPs were used due to their excellent low-field magnetic response. Moreover, the MNPs system has high magnetization saturation which, in association with ACB system configuration of magnetic field of 2 mT and frequency of 10 kHz, presents high magnetic susceptibility and consequently a good detection. Additionally, the Cit-$MnFe_2O_4$ MNPs present suitable properties towards to magnetic hyperthermia [48,49].

Under the perspective to ensure safety future in vivo applications, it is still mandatory to assess the MNPs' time-dependent biodistribution and clearance [50,51]. In this way, our results for Ci-$MnFe_2O_4$ MNPs distribution and clearance made it possible to observe a predominant retention profile in the liver and spleen. The highest uptake of both organs is mainly due to morphophysiological characteristics combined with specialized structures for filtration and retention in these organs.

As can be seen 15 days after the administration, the concentration of MNPs over time in the spleen showed a slight increase in its concentration, which may be correlated with the same rise in liver concentration, indicating that the two organs can act similarly, most likely due to their characteristics.

We also quantified the two half-lives of the liver elimination and the spleen half-life elimination through the pharmacokinetic assessment. Regarding the hepatic clearance, the elimination time was evaluated by a two-phase $T_{1/2}$. The first half-life found can be assigned to the primary MNPs filtration performed by the liver, which captured a high MNP amount. The following half-life reflects the bi-exponential exchange that the liver and bloodstream carry out where part of the MNP returns to the bloodstream. On the other hand, the spleen presented only a phase $T_{1/2}$, characterized by an intense decay. Despite being a highly perfused organ and its high number of macrophages, the spleen did not show the same clearance behavior as the liver; we noticed that around the second post-MNP day injection, the spleen eliminated most particles at once.

MNPs were significantly detected in the blood in the first hour after administration. However, we found no MNPs in the blood four hours after injection, which may be

correlated with the first depuration of the MPS system, removing most of the circulating particles. Quini et al., 2017 [25] showed no signal in the blood four hours after MNPs infusion. This behavior suggests that all MNPs have already been captured by organs or tissue at this time. The low intensity of MNPs present in the heart, and its subsequent decay four hours after administration, can be related to the presence of particles, in the same time interval, in the blood. The absence of MNPs in the heart may be related to particles in the bloodstream and the heart's characteristics, as it does not present retention characteristics. Although the heart is an excessively irrigated organ, the corona effect in the blood may be responsible for avoiding the internalization of MNPs by cardiac cells.

Despite being highly perfused and with their own resident macrophages (myeloid cells residing in renal tissue and alveolar macrophages in the lung tissue) [52,53], the kidneys and the lungs presented a considerably lower signal intensity than the spleen and liver. Studies showed that, despite the morphological characteristics of both organs, there is a dimensional and surface charge dependence for MNPs uptake, which did not contribute to MNP uptake by the liver and lungs. It was also hypothesized that a group of proteins could have bound to the MNP surface, improving the corona protein, which increased their size and facilitated the recognition and the subsequent molecular interactions with the hepatic and splenic structure.

In our finding, it was noticed a decrease in the ACB signal over the time analyzed, which can be directly associated with the MNP state several days after the administration. From this, it is noteworthy that the ACB system is strongly affected by the MNP condition. Therefore, the signal decrease would be explained by inhibiting the Brownian relaxation due to the arrangement of proteins around the MNP surface, resulting in altered magnetic susceptibility. Concomitantly, it is noticeable that partial metabolization after a few days of the MNP infusion also influences the ACB signal and contributes to the signal decrease once the ACB system can detect the MNP in its molecular form, so that no metabolites or ions from MNPs could be seen. The MNP partial metabolization process can be verified through Figure 5, in which was detected around 14% of the injected dose in the final measurement period. It was considered that most MNPs were metabolized or degraded by biological mechanisms that induced changes in the magnetic properties of nanoparticles.

Long-term biodistribution studies illustrate the difficulty of eliminating nanostructured materials when administered to the body, reinforcing the importance of this study modality for future clinical applications of MNPs. Table 1 summarizes studies dedicated to monitoring the MNP's long-term biodistribution and the respective animal models and methodologies used.

Table 1. Studies employed on assessment of the MNPs long-term biodistribution.

MNPs	Species	Dose	Time Post-Injection Assessed	Method/Technique	Ref.
DMSA-coated magnetite	C57BL/6 mice	15 mg Fe kg^{-1}	90 days	Quantum Design MPMS-XL SQUID magnetometer/ICP-AES	[54]
DMSA/PEG Magnetite DMSA	Wistar rats	2.5 mg Fe/kg B.W	30 days	ICP-OES	[55]
Carboxyl coated Iron Oxide	KunMing mice	20 mg kg^{-1}	7 days	Atomic absorption spectroscopy	[56]

Table 1. *Cont.*

MNPs	Species	Dose	Time Post-Injection Assessed	Method/Technique	Ref.
Dextran-coated iron oxide nanoparticles	C3H mice	2 mg Fe/mouse	580 days	Histological analysis/ICP-MS	[32]
Citrate coated $MnFe_2O_4$	Wistar rats	Multiple injections of 6.9 mg/rat	24 h	AC Biosusceptometry/Electron spin resonance	[25]
Dextran-coated magnetite	Swiss mice	100 µL (1×10^{17} particle/mL)	6 months	Magnetic resonance	[52]
Curcumin capped iron oxide nanoparticles	Balb/c mic	5 mg kg^{-1}	3 weeks	Atomic absorption spectroscopy.	[8]
Maghemite coated by hydrophilic derivatives of glucose	mice (C57-B6 mice)	1000 µmol of iron kg^{-1} and 50 µmol of iron kg^{-1}	3 months	EPR and SQUID	[53]
Maghemite (γ-Fe2O3)	Swiss mice	2.4 mg iron	28 days	ICP OES and histological methods.	[57]
γ-Fe2O3 s-SPION	Nude mice (BALB/c-Foxn1nu/Arc)	90 mg Fe kg^{-1}	7 days	Atomic absorption spectroscopy (AAS) and Prussian blue	[33]
Dextran-Iron oxide nanoparticles	Wistar rats	10 mg kg^{-1}	28 days	ICP-AES	[58]
Iron oxide nanoparticles	BALB/c mice	5 mg/mL	24 h	ICP-MS	[7]
Dextran-coated magnetite	Swiss mice	100 µL/mice	6 months	Magnetic resonance	[59]
Iron oxide NPs (Fe_2O_3)	Wistar rats	7.5 mg/kg, 15 mg/kg and 30 mg/kg	28 days	Atomic absorption spectroscopy (AAS)	[60]
Ferucarbotran	Fisher 344 female rats	5 mg Fe/kg	70 days	MPI	[61]

As depicted in Table 1, several approaches have been used to assess the accumulation of different MNPs. Regardless of the type of MNPs, these nanomaterials were detected mainly in the livers of different species over days and months.

Mejías et al., 2013 [54] detected iron oxide MNPs within a period of 30 min to 90 days. However, this study did not establish the total elimination period as, at 90 days, significant amounts of MNPs were still present in the organs. Similar to our findings, Ruiz et al., 2015 [55] analyzed the biodistribution of magnetite nanoparticles up to 30 days post-administration. The study could observe a significant accumulation of MNPs in organs such as the liver, spleen, and lung within 30 days. In another study, Yang and collaborators also found a high concentration of iron seven days after administration of iron oxide nanoparticles in organs such as the liver, spleen, and kidneys [56]. Nonetheless, analyses based on Fe concentrations can induce a series of variations, mainly due to the endogenous iron itself and that MNP may have been metabolized, presenting only an ionic form.

On the other hand, Tate et al., 2011 [32] carried out a long-term assessment in which the authors reported the presence of iron oxide nanoparticles in the liver 580 days after the injection. Other studies also examined the distribution patterns of the non-magnetic

nanoparticles and found significant nanoparticles amounts more than one month in organs responsible for the elimination process.

In this way, we must take into consideration that the MNPs are not eliminated simply as common drugs, as they can remain in the body for months according to our evaluation and literature data. MNPs' time course assessments become crucial to provide the MNPs as a promising material for imaging and therapy applications in medicine.

5. Conclusions

Cit-$MnFe_2O_4$ MNPs were primarily accumulated in the liver and spleen due to these organs' morphological and physiological characteristics and the intrinsic MNPs characteristics.

The data obtained made it possible to observe a concentration decay profile over the 60 days, which suggests that, in addition to elimination via feces, there is an endogenous mechanism of metabolization or possible agglomeration of MNPs, resulting in loss of ACB signal intensity. Furthermore, the clearance profile for MNPs was assessed over the measured period.

The ACB system offers a low-cost, portable, and versatile alternative for evaluating the biodistribution and elimination of MNPs, even at low concentrations. Regarding elimination, the data presented in this work suggest that the MNPs used demonstrated a constant elimination rate that starts from 48 h via feces, which can assist in providing strategies to target drug delivery to specific cell types and consolidate them as agents for magnetic hyperthermia.

Even with the clearance and elimination studies, future studies are required to deeply elucidate the toxicity and the specific elimination mechanisms, aggregation, and metabolization of MNPs. Additionally, the ACB system is a feasible methodology to be employed with different modalities to understand the mechanism of metabolization and clearance of MNPs fully.

Supplementary Materials: The following are available online at https://www.mdpi.com/article/10.3390/ma15062121/s1, Figure S1: TEM images for the magnetic nanoparticles. Scale: (Upper) 100 and (Lower) 10 nm, Figure S2: Particles size distribution, Figure S3: Hydrodynamic distribution for the magnetic nanoparticles, Figure S4: Magnetization curve of the manganese-ferrite nanoparticles, Figure S5: X-ray diffraction pattern of the citrate-coated manganese-ferrite nanoparticles. References [62,63] are sited in the supplementary materials.

Author Contributions: Conceptualization, G.A.S., L.A.P., J.V.C.F., and J.R.A.M.; methodology, G.M.P. and A.G.P.; software, L.P.B., A.G.P., and L.A.P.; validation, J.V.C.F., E.G.S., and G.M.P.; formal analysis, G.A.S., L.A.P., and E.G.S.; investigation., L.P.B., G.M.P., and G.A.S.; resources, G.A.S., L.A.P., L.P.B., and E.G.S.; data writing—original draft preparation, G.A.S., J.V.C.F., L.A.P., and O.B.; writing—review and editing, G.A.S., A.G.P., A.F.B., and J.R.A.M.; supervision, O.B., A.F.B., J.R.A.M., and A.G.P.; project administration, O.B., A.F.B., and J.R.A.M.; and funding acquisition, J.R.A.M., O.B., and A.F.B. All authors have read and agreed to the published version of the manuscript.

Funding: This work was supported by the Fundação de Amparo à Pesquisa do Estado de São Paulo (FAPESP) Grants 2021/09829-4, 2019/11277-0 and 2013/07699–0. It was supported by the Conselho Nacional de Pesquisas e Desenvolvimento Tecnológico (CNPq) Grants 304107/2019-0, 312074/2018-9 and 311074/2018-9.

Institutional Review Board Statement: The study was conducted and approved by the the São Paulo State University (UNESP) Committee for the Use and Care of Animals (protocol no. CEUA—IBB 1135).

Informed Consent Statement: Not applicable.

Data Availability Statement: Almost all data are presented within the manuscript (Figures and Tables). The raw data presented in this study are available on request from the corresponding author.

Acknowledgments: The support by the German Academic Exchange program DAAD in cooperation with Brazilian CAPES- PROBRAL (project ID 57446914, 88887.198747/2018-00 & 888 81.198748/2018-01) is kindly acknowledged.

Conflicts of Interest: The authors declare no conflict of interest.

References

1. Anderson, S.D.; Gwenin, V.V.; Gwenin, C.D. Magnetic Functionalized Nanoparticles for Biomedical, Drug Delivery and Imaging Applications. *Nanoscale Res. Lett.* **2019**, *14*, 188. [CrossRef]
2. Sehl, O.C.; Gevaert, J.J.; Melo, K.P.; Knier, N.N.; Foster, P.J. A perspective on cell tracking with magnetic particle imaging. *Tomography* **2020**, *6*, 315–324. [CrossRef]
3. Avasthi, A.; Caro, C.; Pozo-Torres, E.; Leal, M.P.; García-Martín, M.L. Magnetic Nanoparticles as MRI Contrast Agents. *Top. Curr. Chem.* **2020**, *378*, 40. [CrossRef] [PubMed]
4. Ashikbayeva, Z.; Aitkulov, A.; Jelbuldina, M.; Issatayeva, A.; Beisenova, A.; Molardi, C.; Saccomandi, P.; Blanc, W.; Inglezakis, V.J.; Tosi, D. Distributed 2D temperature sensing during nanoparticles assisted laser ablation by means of high-scattering fiber sensors. *Sci. Rep.* **2020**, *10*, 12593. [CrossRef] [PubMed]
5. Cardoso, V.F.; Francesko, A.; Ribeiro, C.; Bañobre-López, M.; Martins, P.; Lanceros-Mendez, S. Advances in magnetic nanoparticles for biomedical applications. *Adv. Healthc. Mater.* **2018**, *7*, 1700845. [CrossRef] [PubMed]
6. Baetke, S.C.; Lammers, T.; Kiessling, F. Applications of nanoparticles for diagnosis and therapy of cancer. *Br. J. Radiol.* **2015**, *88*, 20150207. [CrossRef] [PubMed]
7. Salimi, M.; Sarkar, S.; Fathi, S.; Alizadeh, A.M.; Saber, R.; Moradi, F.; Delavari, H. Biodistribution, pharmacokinetics, and toxicity of dendrimer-coated iron oxide nanoparticles in BALB/c mice. *Int. J. Nanomed.* **2018**, *13*, 1483. [CrossRef]
8. Elbialy, N.S.; Aboushoushah, S.F.; Alshammari, W.W. Long-term biodistribution and toxicity of curcumin capped iron oxide nanoparticles after single-dose administration in mice. *Life Sci.* **2019**, *230*, 76–83. [CrossRef] [PubMed]
9. Hua, S.; de Matos, M.B.C.; Metselaar, J.M.; Storm, G. Current Trends and Challenges in the Clinical Translation of Nanoparticulate Nanomedicines: Pathways for Translational Development and Commercialization. *Front. Pharmacol.* **2018**, *9*. [CrossRef]
10. Kudr, J.; Haddad, Y.; Richtera, L.; Heger, Z.; Cernak, M.; Adam, V.; Zitka, O. Magnetic Nanoparticles: From Design and Synthesis to Real World Applications. *Nanomaterials* **2017**, *7*, 243. [CrossRef]
11. Huang, H.S.; Hainfeld, J.F. Intravenous magnetic nanoparticle cancer hyperthermia. *Int. J. Nanomed.* **2013**, *8*, 2521–2532.
12. Feng, Q.; Liu, Y.; Huang, J.; Chen, K.; Huang, J.; Xiao, K. Uptake, distribution, clearance, and toxicity of iron oxide nanoparticles with different sizes and coatings. *Sci. Rep.* **2018**, *8*, 2082. [CrossRef] [PubMed]
13. Arami, H.; Khandhar, A.; Liggitt, D.; Krishnan, K.M. In vivo delivery, pharmacokinetics, biodistribution and toxicity of iron oxide nanoparticles. *Chem. Soc. Rev.* **2015**, *44*, 8576–8607. [CrossRef]
14. Colino, C.I.; Lanao, J.M.; Gutierrez-Millan, C. Targeting of Hepatic Macrophages by Therapeutic Nanoparticles. *Front. Immunol.* **2020**, *11*, 218. [CrossRef]
15. Ma, Y.; Cai, F.; Li, Y.; Chen, J.; Han, F.; Lin, W. A review of the application of nanoparticles in the diagnosis and treatment of chronic kidney disease. *Bioact. Mater.* **2020**, *5*, 732–743. [CrossRef] [PubMed]
16. Poller, W.C.; Löwa, N.; Wiekhorst, F.; Taupitz, M.; Wagner, S.; Möller, K.; Baumann, G.; Stangl, V.; Trahms, L.; Ludwig, A. Magnetic particle spectroscopy reveals dynamic changes in the magnetic behavior of very small superparamagnetic iron oxide nanoparticles during cellular uptake and enables determination of cell-labeling efficacy. *J. Biomed. Nanotechnol.* **2016**, *12*, 337–346. [CrossRef]
17. De Jong, W.H.; Hagens, W.I.; Krystek, P.; Burger, M.C.; Sips, A.J.; Geertsma, R.E.J.B. Particle size-dependent organ distribution of gold nanoparticles after intravenous administration. *Biomaterials* **2008**, *29*, 1912–1919. [CrossRef]
18. Baboci, L.; Capolla, S.; Di Cintio, F.; Colombo, F.; Mauro, P.; Dal Bo, M.; Argenziano, M.; Cavalli, R.; Toffoli, G.; Macor, P. The Dual Role of the Liver in Nanomedicine as an Actor in the Elimination of Nanostructures or a Therapeutic Target. *J. Oncol.* **2020**, *2020*, 4638192. [CrossRef]
19. Yu, Q.; Xiong, X.-q.; Zhao, L.; Xu, T.-t.; Bi, H.; Fu, R.; Wang, Q.-h. Biodistribution and Toxicity Assessment of Superparamagnetic Iron Oxide Nanoparticles In Vitro and In Vivo. *Curr. Med. Sci.* **2018**, *38*, 1096–1102. [CrossRef] [PubMed]
20. Couto, D.; Freitas, M.; Costa, V.M.; Chisté, R.C.; Almeida, A.; Lopez-Quintela, M.A.; Rivas, J.; Freitas, P.; Silva, P.; Carvalho, F. Biodistribution of polyacrylic acid-coated iron oxide nanoparticles is associated with proinflammatory activation and liver toxicity. *J. Appl. Toxicol.* **2016**, *36*, 1321–1331. [CrossRef] [PubMed]
21. Poon, W.; Zhang, Y.-N.; Ouyang, B.; Kingston, B.R.; Wu, J.L.; Wilhelm, S.; Chan, W.C. Elimination pathways of nanoparticles. *Acs Nano* **2019**, *13*, 5785–5798. [CrossRef] [PubMed]
22. Soares, G.; Prospero, A.; Calabresi, M.; Rodrigues, D.; Simoes, L.; Quini, C.; Matos, R.; Pinto, L.; Sousa, A.; Bakuzis, A.; et al. Multichannel AC Biosusceptometry system to map biodistribution and assess the pharmacokinetic profile of magnetic nanoparticles by imaging. *IEEE Trans. Nanobioscience* **2019**, *18*, 456–462. [CrossRef] [PubMed]
23. Próspero, A.G.; Soares, G.A.; Moretto, G.M.; Quini, C.C.; Bakuzis, A.F.; de Arruda Miranda, J.R. Dynamic cerebral perfusion parameters and magnetic nanoparticle accumulation assessed by AC biosusceptometry. *Biomed. Eng./Biomed. Tech.* **2020**, *65*, 343–351. [CrossRef]
24. Próspero, A.G.; Quini, C.C.; Bakuzis, A.F.; Fidelis-de-Oliveira, P.; Moretto, G.M.; Mello, F.P.F.; Calabresi, M.F.F.; Matos, R.V.R.; Zandoná, E.A.; Zufelato, N.; et al. Real-time in vivo monitoring of magnetic nanoparticles in the bloodstream by AC biosusceptometry. *J. Nanobiotechnol.* **2017**, *15*, 22. [CrossRef]
25. Quini, C.C.; Próspero, A.G.; Calabresi, M.F.F.; Moretto, G.M.; Zufelato, N.; Krishnan, S.; Pina, D.R.; Oliveira, R.B.; Baffa, O.; Bakuzis, A.F.; et al. Real-time liver uptake and biodistribution of magnetic nanoparticles determined by AC biosusceptometry. *Nanomed. Nanotechnol. Biol. Med.* **2017**, *13*, 1519–1529. [CrossRef] [PubMed]

26. Cataldi, M.; Vigliotti, C.; Mosca, T.; Cammarota, M.; Capone, D. Emerging role of the spleen in the pharmacokinetics of monoclonal antibodies, nanoparticles and exosomes. *Int. J. Mol. Sci.* **2017**, *18*, 1249. [CrossRef]
27. Franken, L.; Klein, M.; Spasova, M.; Elsukova, A.; Wiedwald, U.; Welz, M.; Knolle, P.; Farle, M.; Limmer, A.; Kurts, C. Splenic red pulp macrophages are intrinsically superparamagnetic and contaminate magnetic cell isolates. *Sci. Rep.* **2015**, *5*, 12940. [CrossRef]
28. Tekie, F.S.M.; Hajiramezanali, M.; Geramifar, P.; Raoufi, M.; Dinarvand, R.; Soleimani, M.; Atyabi, F. Controlling evolution of protein corona: A prosperous approach to improve chitosan-based nanoparticle biodistribution and half-life. *Sci. Rep.* **2020**, *10*, 9664. [CrossRef]
29. Dutz, S.; Weidner, A.; von der Lühe, M.; Gräfe, C.; Biehl, P.; Demut, J.; Warncke, P.; Jungmann, S.; Fischer, D.; Schacher, F.H. Hybrid nanomaterials of biomolecule corona coated magnetic nanoparticles and their interaction with biological systems. *Phys. Sci. Rev.* **2020**, *2020*, 20190110. [CrossRef]
30. Chiu, C.-Y.; Chung, T.-W.; Chen, S.-Y.; Ma, Y.-H. Effects of PEGylation on capture of dextran-coated magnetic nanoparticles in microcirculation. *Int. J. Nanomed.* **2019**, *14*, 4767. [CrossRef] [PubMed]
31. Prospero, A.G.; Buranello, L.P.; Fernandes, C.A.; Dos Santos, L.D.; Soares, G.; C Rossini, B.; Zufelato, N.; Bakuzis, A.F.; de Mattos Fontes, M.R.; de Arruda Miranda, J.R. Corona protein impacts on alternating current biosusceptometry signal and circulation times of differently coated MnFe2O4 nanoparticles. *Nanomedicine* **2021**, *16*, 2189–2206. [CrossRef] [PubMed]
32. Tate, J.A.; Petryk, A.A.; Giustini, A.J.; Hoopes, P.J. In vivo biodistribution of iron oxide nanoparticles: An overview. *Energy-Based Treat. Tissue Assess. VI* **2011**, *7901*, 790117.
33. Pham, B.T.; Colvin, E.K.; Pham, N.T.; Kim, B.J.; Fuller, E.S.; Moon, E.A.; Barbey, R.; Yuen, S.; Rickman, B.H.; Bryce, N.S. Biodistribution and clearance of stable superparamagnetic maghemite iron oxide nanoparticles in mice following intraperitoneal administration. *Int. J. Mol. Sci.* **2018**, *19*, 205. [CrossRef] [PubMed]
34. Zelepukin, I.V.; Yaremenko, A.V.; Ivanov, I.N.; Yuryev, M.V.; Cherkasov, V.R.; Deyev, S.M.; Nikitin, P.I.; Nikitin, M.P. Long-Term Fate of Magnetic Particles in Mice: A Comprehensive Study. *ACS Nano* **2021**, *15*, 11341–11357. [CrossRef]
35. Prodan, A.M.; Iconaru, S.L.; Ciobanu, C.S.; Chifiriuc, M.C.; Stoicea, M.; Predoi, D. Iron oxide magnetic nanoparticles: Characterization and toxicity evaluation by in vitro and in vivo assays. *J. Nanomater.* **2013**, *2013*, 587021.
36. Storey, P.; Lim, R.P.; Chandarana, H.; Rosenkrantz, A.B.; Kim, D.; Stoffel, D.R.; Lee, V.S. MRI Assessment of Hepatic Iron Clearance Rates After USPIO Administration in Healthy Adults. *Investig. Radiol.* **2012**, *47*, 717–724. [CrossRef] [PubMed]
37. Wang, Y.-X.J. Current status of superparamagnetic iron oxide contrast agents for liver magnetic resonance imaging. *World J. Gastroenterol.* **2015**, *21*, 13400–13402. [CrossRef]
38. Patra, J.K.; Das, G.; Fraceto, L.F.; Campos, E.V.R.; Rodriguez-Torres, M.d.P.; Acosta-Torres, L.S.; Diaz-Torres, L.A.; Grillo, R.; Swamy, M.K.; Sharma, S.; et al. Nano based drug delivery systems: Recent developments and future prospects. *J. Nanobiotechnology* **2018**, *16*, 71. [CrossRef]
39. Anselmo, A.C.; Mitragotri, S. Nanoparticles in the clinic: An update. *Bioeng. Transl. Med.* **2019**, *4*, e10143. [CrossRef] [PubMed]
40. Wahsner, J.; Gale, E.M.; Rodríguez-Rodríguez, A.; Caravan, P. Chemistry of MRI contrast agents: Current challenges and new frontiers. *Chem. Rev.* **2018**, *119*, 957–1057. [CrossRef]
41. Stueber, D.D.; Villanova, J.; Aponte, I.; Xiao, Z.; Colvin, V.L. Magnetic Nanoparticles in Biology and Medicine: Past, Present, and Future Trends. *Pharmaceutics* **2021**, *13*, 943. [CrossRef]
42. Nosrati, H.; Salehiabar, M.; Davaran, S.; Danafar, H.; Manjili, H.K. Methotrexate-conjugated L-lysine coated iron oxide magnetic nanoparticles for inhibition of MCF-7 breast cancer cells. *Drug Dev. Ind. Pharm.* **2018**, *44*, 886–894. [CrossRef] [PubMed]
43. Bobo, D.; Robinson, K.J.; Islam, J.; Thurecht, K.J.; Corrie, S.R. Nanoparticle-Based Medicines: A Review of FDA-Approved Materials and Clinical Trials to Date. *Pharm. Res.* **2016**, *33*, 2373–2387. [CrossRef] [PubMed]
44. Moonen, R.P.M.; Coolen, B.F.; Sluimer, J.C.; Daemen, M.J.A.P.; Strijkers, G.J. Iron Oxide Nanoparticle Uptake in Mouse Brachiocephalic Artery Atherosclerotic Plaque Quantified by T2-Mapping MRI. *Pharmaceutics* **2021**, *13*, 279. [CrossRef]
45. Bulte, J.W.M. Superparamagnetic iron oxides as MPI tracers: A primer and review of early applications. *Adv. Drug Deliv. Rev.* **2019**, *138*, 293–301. [CrossRef]
46. Paysen, H.; Loewa, N.; Stach, A.; Wells, J.; Kosch, O.; Twamley, S.; Makowski, M.R.; Schaeffter, T.; Ludwig, A.; Wiekhorst, F. Cellular uptake of magnetic nanoparticles imaged and quantified by magnetic particle imaging. *Sci. Rep.* **2020**, *10*, 1922. [CrossRef] [PubMed]
47. Quini, C.C.; Próspero, A.G.; Kondiles, B.R.; Chaboub, L.; Hogan, M.K.; Baffa, O.; Bakuzis, A.F.; Horner, P.J.; Miranda, J.R.A. Development of a protocol to assess cell internalization and tissue uptake of magnetic nanoparticles by AC Biosusceptometry. *J. Magn. Magn. Mater.* **2019**, *473*, 527–533. [CrossRef]
48. Aquino, V.; Vinícius-Araújo, M.; Shrivastava, N.; Sousa, M.; Coaquira, J.; Bakuzis, A. Role of the fraction of blocked nanoparticles on the hyperthermia efficiency of Mn-based ferrites at clinically relevant conditions. *J. Phys. Chem. C* **2019**, *123*, 27725–27734. [CrossRef]
49. Rodrigues, H.F.; Mello, F.M.; Branquinho, L.C.; Zufelato, N.; Silveira-Lacerda, E.P.; Bakuzis, A.F. Real-time infrared thermography detection of magnetic nanoparticle hyperthermia in a murine model under a non-uniform field configuration. *Int. J. Hyperth.* **2013**, *29*, 752–767. [CrossRef] [PubMed]
50. Malhotra, N.; Lee, J.-S.; Liman, R.A.D.; Ruallo, J.M.S.; Villaflores, O.B.; Ger, T.-R.; Hsiao, C.-D. Potential toxicity of iron oxide magnetic nanoparticles: A review. *Molecules* **2020**, *25*, 3159. [CrossRef]

51. Senthilkumar, N.; Sharma, P.K.; Sood, N.; Bhalla, N. Designing magnetic nanoparticles for in vivo applications and understanding their fate inside human body. *Coord. Chem. Rev.* **2021**, *445*, 214082. [CrossRef]
52. Estevanato, L.L.; Lacava, L.M.; Carvalho, L.C.; Azevedo, R.B.; Silva, O.; Pelegrini, F.; Báo, S.N.; Morais, P.C.; Lacava, Z.G. Long-term biodistribution and biocompatibility investigation of dextran-coated magnetite nanoparticle using mice as the animal model. *J. Biomed. Nanotechnol.* **2012**, *8*, 301–308. [CrossRef]
53. Levy, M.; Luciani, N.; Alloyeau, D.; Elgrabli, D.; Deveaux, V.; Pechoux, C.; Chat, S.; Wang, G.; Vats, N.; Gendron, F.; et al. Long term in vivo biotransformation of iron oxide nanoparticles. *Biomaterials* **2011**, *32*, 3988–3999. [CrossRef] [PubMed]
54. Mejías, R.; Gutiérrez, L.; Salas, G.; Pérez-Yagüe, S.; Zotes, T.M.; Lázaro, F.J.; Morales, M.P.; Barber, D.F. Long term biotransformation and toxicity of dimercaptosuccinic acid-coated magnetic nanoparticles support their use in biomedical applications. *J. Control. Release* **2013**, *171*, 225–233. [CrossRef] [PubMed]
55. Ruiz, A.; Gutiérrez, L.; Cáceres-Vélez, P.R.; Santos, D.; Chaves, S.B.; Fascineli, M.L.; Garcia, M.P.; Azevedo, R.B.; Morales, M.P. Biotransformation of magnetic nanoparticles as a function of coating in a rat model. *Nanoscale* **2015**, *7*, 16321–16329. [CrossRef]
56. Yang, L.; Kuang, H.; Zhang, W.; Aguilar, Z.P.; Xiong, Y.; Lai, W.; Xu, H.; Wei, H. Size dependent biodistribution and toxicokinetics of iron oxide magnetic nanoparticles in mice. *Nanoscale* **2015**, *7*, 625–636. [CrossRef] [PubMed]
57. Pinheiro, W.O.; Fascineli, M.L.; Farias, G.R.; Horst, F.H.; de Andrade, L.R.; Corrêa, L.H.; Magalhães, K.G.; Sousa, M.H.; de Almeida, M.C.; Azevedo, R.B. The influence of female mice age on biodistribution and biocompatibility of citrate-coated magnetic nanoparticles. *Int. J. Nanomed.* **2019**, *14*, 3375. [CrossRef]
58. Easo, S.; Neelima, R.; Mohanan, P.V. Toxicokinetics and biodistribution of dextran stabilized iron oxide nanoparticles in rats. *Mater. Res. Express* **2015**, *2*, 075401. [CrossRef]
59. Lacava, L.; Garcia, V.; Kückelhaus, S.; Azevedo, R.; Sadeghiani, N.; Buske, N.; Morais, P.; Lacava, Z. Long-term retention of dextran-coated magnetite nanoparticles in the liver and spleen. *J. Magn. Magn. Mater.* **2004**, *272*, 2434–2435. [CrossRef]
60. Gaharwar, U.S.; Meena, R.; Rajamani, P. Biodistribution, Clearance And Morphological Alterations Of Intravenously Administered Iron Oxide Nanoparticles In Male Wistar Rats. *Int. J. Nanomed.* **2019**, *14*, 9677–9692. [CrossRef]
61. Keselman, P.; Elaine, Y.Y.; Zhou, X.Y.; Goodwill, P.W.; Chandrasekharan, P.; Ferguson, R.M.; Khandhar, A.P.; Kemp, S.J.; Krishnan, K.M.; Zheng, B.J.; et al. Tracking short-term biodistribution and long-term clearance of SPIO tracers in magnetic particle imaging. *Phys. Med. Biol.* **2017**, *62*, 3440. [CrossRef] [PubMed]
62. Quini, C.C.; Matos, J.F.; Próspero, A.G.; Calabresi, M.F.F.; Zufelato, N.; Bakuzis, A.F.; Baffa, O.; Miranda, J.R.A. Renal perfusion evaluation by alternating current biosusceptometry of magnetic nanoparticles. *J. Magn. Magn. Mater.* **2015**, *380*, 2–6. [CrossRef]
63. Nunes, A.D.; Ramalho, L.S.; Souza, Á.P.; Mendes, E.P.; Colugnati, D.B.; Zufelato, N.; Sousa, M.H.; Bakuzis, A.F.; Castro, C.H. Manganese ferrite-based nanoparticles induce ex vivo, but not in vivo, cardiovascular effects. *Int. J. Nanomedicine.* **2014**, *9*, 3299–3312.

CAPÍTULO III

Biodistribution Profile of Magnetic Nanoparticles in Cirrhosis-Associated Hepatocarcinogenesis in Rats by AC Biosusceptometry

pharmaceutics

MDPI

Article

Biodistribution Profile of Magnetic Nanoparticles in Cirrhosis-Associated Hepatocarcinogenesis in Rats by AC Biosusceptometry

Guilherme A. Soares [1,*], Gabriele M. Pereira [1], Guilherme R. Romualdo [2,3], Gabriel G. A. Biasotti [1], Erick G. Stoppa [1], Andris F. Bakuzis [4], Oswaldo Baffa [5], Luis F. Barbisan [3] and Jose R. A. Miranda [1]

1 Department of Biophysics and Pharmacology, Institute of Biosciences, São Paulo State University—UNESP, Botucatu 18618-689, SP, Brazil
2 Department of Pathology, Botucatu Medical School, São Paulo State University (UNESP), Botucatu 18618-689, SP, Brazil
3 Department of Strucutral and Functional Biology, Institute of Biosciences, São Paulo State University—UNESP, Botucatu 18618-689, SP, Brazil
4 Institute of Physics, Federal University of Goiás, Goiânia 74690-900, GO, Brazil
5 Faculty of Philosophy, Sciences and Letters at Ribeirão Preto, University of São Paulo, Ribeirão Preto 14040-900, SP, Brazil
* Correspondence: guilherme.soares@unesp.br

Citation: Soares, G.A.; Pereira, G.M.; Romualdo, G.R.; Biasotti, G.G.A.; Stoppa, E.G.; Bakuzis, A.F.; Baffa, O.; Barbisan, L.F.; Miranda, J.R.A. Biodistribution Profile of Magnetic Nanoparticles in Cirrhosis-Associated Hepatocarcinogenesis in Rats by AC Biosusceptometry. *Pharmaceutics* **2022**, *14*, 1907. https://doi.org/10.3390/pharmaceutics14091907

Academic Editors: Francesca Garello, Bogdan Parakhonskiy, Miriam Filippi and Yulia I. Svenskaya

Received: 11 July 2022
Accepted: 31 August 2022
Published: 8 September 2022

Abstract: Since magnetic nanoparticles (MNPs) have been used as multifunctional probes to diagnose and treat liver diseases in recent years, this study aimed to assess how the condition of cirrhosis-associated hepatocarcinogenesis alters the biodistribution of hepatic MNPs. Using a real-time image acquisition approach, the distribution profile of MNPs after intravenous administration was monitored using an AC biosusceptometry (ACB) assay. We assessed the biodistribution profile based on the ACB images obtained through selected regions of interest (ROIs) in the heart and liver position according to the anatomical references previously selected. The signals obtained allowed for the quantification of pharmacokinetic parameters, indicating that the uptake of hepatic MNPs is compromised during liver cirrhosis, since scar tissue reduces blood flow through the liver and slows its processing function. Since liver monocytes/macrophages remained constant during the cirrhotic stage, the increased intrahepatic vascular resistance associated with impaired hepatic sinusoidal circulation was considered the potential reason for the change in the distribution of MNPs.

Keywords: AC biosuceptometry; magnetic nanoparticles; cirrhosis-associated rat hepatocarcinogenesis; nanotechnology

1. Introduction

The liver is a solid organ that is divided into two portions: (1) a parenchymal portion, which is composed of hepatocytes and biliary cells, and (2) a non-parenchymal portion, constituted by Kupffer cells (KCs), sinusoidal endothelial cells (LSECs), and resting hepatic stellate cells (HSCs) [1]. The KCs are resident macrophages that specialize in phagocytosis and cytokine release, acting as the liver's first immune defense [2]. KCs are associated with the LSECs that line the hepatic sinusoids. The HSCs are spread throughout the Disse space and are responsible for storing vitamin A and secreting limited amounts of extracellular matrix (ECM) proteins under physiological conditions [3].

The liver, under homeostasis, displays an extensive range of functions, such as the regulation of blood volume and immunity, drug detoxification, endocrine control of growth, lipid and cholesterol homeostasis, and the metabolism of nutrients. It also features a regenerative capacity through hepatocytes [4–6] Nonetheless, this organ may develop several chronic diseases, including non-neoplastic and neoplastic diseases. Hepatocellular

carcinoma (HCC), the main primary hepatic malignancy, stands out for its current epidemiological burden, as it ranks fourth among the most common cancers and it is the sixth most common cause of cancer-related deaths worldwide [7]. HCC usually emerges in the context of hepatic fibrosis/cirrhosis (70–95% of cases) [8] and also features a poor prognosis, with a median survival time of 11 months and survival rates of 19 to 29% at 3 years after diagnosis [9,10]. Furthermore, a 53% to 60% growth in both the incidence of and mortality from HCC is estimated over the next 20 years [7]. Such epidemiological data elicit the need for new diagnostic, preventative, and therapeutic tools for this malignance.

Under the known risk conditions—i.e., chronic hepatitis B and C infections, non-alcoholic liver disease, and alcohol intake—HCC gradually emerges in the context of tumor-promoting inflammation/hepatocyte injury hallmarks, HSC activation, and HSC sand macrophage pro-inflammatory crosstalk, culminating on collagen production. Collagen progressively accumulates, leading to liver fibrosis, and the end stage of this process is called cirrhosis, which is characterized by a marked impairment of liver function and an increased risk for HCC development [11]. In order to investigate the different aspects of cirrhosis-associated hepatocarcinogenesis, experimental models, including chemically induced models, have been widely applied in translational research [11–14]. These models use chemical hepatotoxins that induce (pre)neoplastic lesions in a cirrhotic background, as in the diethylnitrosamine (DEN)-initiated and thioacetamide (TAA)-promoted model [15]. These murine models gather morphological and molecular similarities to the corresponding human disease, enabling translational research on hepatocarcinogenesis [11,13] and nanotechnology studies.

Despite liver fibrosis not having clear symptoms, its early detection is essential for preventing the further aggravation to other diseases such as cirrhosis and HCC and for providing beneficial future treatments [14,15]. Although a percutaneous liver biopsy is an invasive strategy and presents several drawbacks, such as sampling error and cost, this diagnostic procedure is usually always associated with non-invasive diagnostic methods and serum biochemistry [16–18]. In addition to non-invasive staging of hepatic fibrosis using magnetic resonance imaging (MRI) and computed tomography (CT), ultrasonography is a widely used accurate diagnostic imaging tool [19–22]. This diagnostic method is also inexpensive, supporting its practical use. Nevertheless, these imaging methods have drawbacks that make detecting fibrosis and cirrhosis at early stages difficult, and there are also drawbacks related to the experience level of the operator. Furthermore, these methods are not indicated for obese patients [18,23]. Despite a routine MRI examination presenting advantages such as its ability to reach deep tissue in the liver with a high spatial resolution, which allows for a complete characterization of liver disease processes, it has some limitations [14]. At the same time, the disadvantages of CTs are the need for ionizing radiation and the existence of respiratory motion artifacts.

Several conventional approaches have been employed to suppress hepatic inflammation/scar deposition using antifibrotic drugs to treat liver diseases. However, most of these conventional therapies are ineffective because the drug delivery is not specific, since specific hepatic cell types are responsible for hepatic inflammation/fibrosis [4,24,25]. In this way, the difficulty of delivering a sufficient dose of pharmacological agents to the liver is associated with the non-specificity of targeting cellular structures, indicating that treating liver diseases remains a challenge.

Nanomaterials have attracted attention in the development of nanotechnology due to the possibility of their use as multifunction probes for diagnoses and treatments in recent years [26–31]. Nanoparticles have great potential for several biomedical applications since they have interesting properties, such as a reduced size, shape manipulation, and the possibility of conjugation with other materials and molecules. A class of nanoparticles that has several advantages due to the intrinsic properties and biocompatibility of its members is magnetic nanoparticles (MNPs). Over the last few years, MNPs have been used in many theranostic applications [32–35], including diagnosing and treating hepatic diseases [32–34]. The magnetic nanoparticle-based diagnosis and treatment of liver diseases has shown

great potential, since MNPs present advantages such as (i) easy functionalization and conjugation with molecules and surface markers, which allows for targeting drug delivery agents to specific cell-type agents [35]; (ii) their ability to act as magnetic vectors to specific liver locations, since they respond strongly to an external magnetic gradient [36]; and (iii) their ability to act as labeling and tracking agents in imaging modalities, thus enhancing non-invasive approaches for investigating liver fibrosis conditions [37,38]. Within the parameters that determine the blood clearance pharmacokinetics of MNPs, the hydrodynamic size of MNPs is one of the most critical parameters that affect their biodistribution kinetics and uptake by the mononuclear phagocyte system (MPS) [39,40]. The MPS, which comprises dendritic cells, blood monocytes, and resident-tissue macrophages in several organs, is a specialized and selective structure that takes up nanoparticles in general. Usually, it has been reported through consistent evidence that nanoparticles presenting with hydrodynamic sizes within 15–100 nm are captured mainly by the liver and the spleen [41–43]. In comparison, nanomaterials smaller than 10 nm are likely to be eliminated through renal clearance [44–46].

Once administered intravenously, MNPs are substantially captured and retained in the liver, depending on physical factors such as coating, dose, and size [47]. The presence of fenestrated vasculature (sinusoids) and many Kupffer cells supports the significant amount of MNPs in the liver. Literature reports have indicated that the liver takes up around 30–99% of the MNPs in a dose [48–51]. Therefore, the high abundance of MNPs in the liver after intravenous injection and their superparamagnetic properties increase the potential of these materials to be used as a contrast agent to enhance the signal-to-noise ratio, which makes magnetic imaging modalities feasible for diagnosing liver diseases [52–55].

Over the years, several methods have been used to detect MNPs in tissues. These methods are classified into direct and indirect methodologies. For in vivo studies, MRI and magnetic particle imaging (MPI) are techniques that detect and visualize particles by their inherent properties and can contribute to determining the pharmacokinetics and biodistribution of MNPs [56].

Despite MRI being a consolidated methodology for imaging, in general, it involves a high cost and also has drawbacks regarding the differentiation of the position of MNPs with a low signal [7].

MPI emerged as an alternative and promising technique for MNP detection. The technique is based on the nonlinear magnetic response of the IONPs to an applied AC magnetic field and presents no depth limitation when used to directly measure the MNP concentration. However, MPI presents limitations regarding the complexity and associated high cost, so it is not widely used [57]. Nanoparticles can be detected through their conjugation to contrast agents or radioactive markers by using imaging methodologies such as near-infrared (NIR) fluorescence, positron emission tomography (PET), and single-photon emission computed tomography (SPECT) [58–60].

Electron paramagnetic resonance (EPR) and a superconducting quantum interference device (SQUID) are magnetometry techniques that are able to carry out ex vivo assessments.

Within ex vivo methodologies, elemental analysis methodologies, such as inductively coupled plasma-atomic emission spectroscopy (ICP-AES) and Prussian blue analysis, show limitations in quantifying the exclusive iron from MNPs [61,62].

An alternate current biosusceptometry (ACB) system has been employed in biological applications involving MNPs because of its unique advantages, such as a low-cost versatility and a lack of specialized equipment required. The system also does not use ionization radiation and works in unshielded magnetic environments [63–67]. Recently, the system has been improved through a comprehensive mathematical and computational approach to quantitatively reconstruct 2D distributions of MNPs [68].

In a previous study, we undertook a pharmacological approach to understand hepatic MNP uptake through ACB imaging. However, the study was limited to quantifying the MNP distribution, potentially minimizing future pre-clinical applications.

We emphasize that the paper presented here represents a significant improvement to the ACB system, mainly regarding MNP quantification in real time using high-quality quantitative images through the inverse problem solution. In addition, this work describes the use of a new MC-ACB system with a higher temporal resolution due to the number and density of detector coils and an additional biodistribution analysis.

Therefore, we decided to implement the MC-ACB system associated with MNPs to investigate a chronic liver disease that significantly impacts morbidity and mortality worldwide.

2. Materials and Methods

2.1. Magnetic Nanoparticles

Solutions of iron (III) chloride hexahydrate ($FeCl_3$—purity 97–100%), manganese (II) chloride tetrahydrate ($MnCl_2$ $4H_2O$—purity 98–100%), iron nitrate (Fe $(NO_3)_3$—purity 98–100%), and methylamine (CH_3NH_2—purity 99.5%) were purchased from Sigma-Aldrich (St. Louis, MO, USA). Acetone (purity 99.6%) and sodium citrate ($Na_3C_6H_5O_7$—purity 99–100%) were purchased from Cromoline, Diadema, Brazil.

We used citrate-coated manganese ferrite nanoparticles (Cit-$MnFe_2O_4$) synthesized by co-precipitation as described before [69,70]. Dynamic light scattering (DLS, Zetasizer NanoS Malvern Instruments, Malvern, UK) measurements showed the hydrodynamic diameter of the particles and zeta potential. Through a Jeol transmission electron microscope, model JEM 2100 (Tokyo, Japan), operating at 200 kV, we obtained images of the core diameter distribution of the MNPs. The magnetization curve of the Cit-$MnFe_2O_4$ MNPs was obtained using an ADE Vibrating Sample Magnetometer (VSM), model EV9 (MicroSense, EastLowell, MA, USA). The Cit-$MnFe_2O_4$ composition was assessed using an energy-dispersive X-ray spectroscopy (EDS) detector (Jeol, JSM-6610).

The X-ray diffraction patterns of the MNP powders were analyzed using a Shimadzu 6000 diffractometer (Shimadzu Corporation, Kyoto, Japan) in order to study the structural parameters of the MNPs. To ensure the success of the coating and confirm the presence of the magnetic nanoparticles, Fourier-transform infrared (FTIR) analysis was carried out using Varian IR 640 equipment.

2.2. Alternate Current Biosusceptometry

The system was a magnetic material detector working as a double magnetic flux transformer, and was composed of 19 drive and pickup coils. Both pairs were arranged on a first-order gradiometer to provide a good signal-to-noise ratio while reducing environmental noise and leading to the cancelation of the common mode. When the magnetic sample was near the pickup coils, the magnetic flux balance was altered, inducing an electric current in the pickup coils proportional to the volume δv and magnetic susceptibility χ.

This signal was acquired using the same low-noise lock-in amplifier that recorded the excitation frequency components (10 kHz). After converting into a direct current signal (DC), the ACB signal was digitalized in real time using a National Instruments A/D board (20 Hz of the sampling rate).

The ACB signal intensity detected by the pickup coils depended on intrinsic coil parameters, such as the area of the detection coil, the number of turns, the magnetic flux change rate, and the amount of magnetic material. Detailed information can be found in [68].

We used two ACB setups for our measurements in this present study. The multichannel ACB system (MC-ACB) was employed to acquire the real-time biodistribution of MNPs simultaneously in blood circulation and the liver. Then, we utilized a suitable ACB sensor to quantify the final mass accumulated in each organ collected after the animal's death [43]. Figure 1 presents the two ACB setups used in this work.

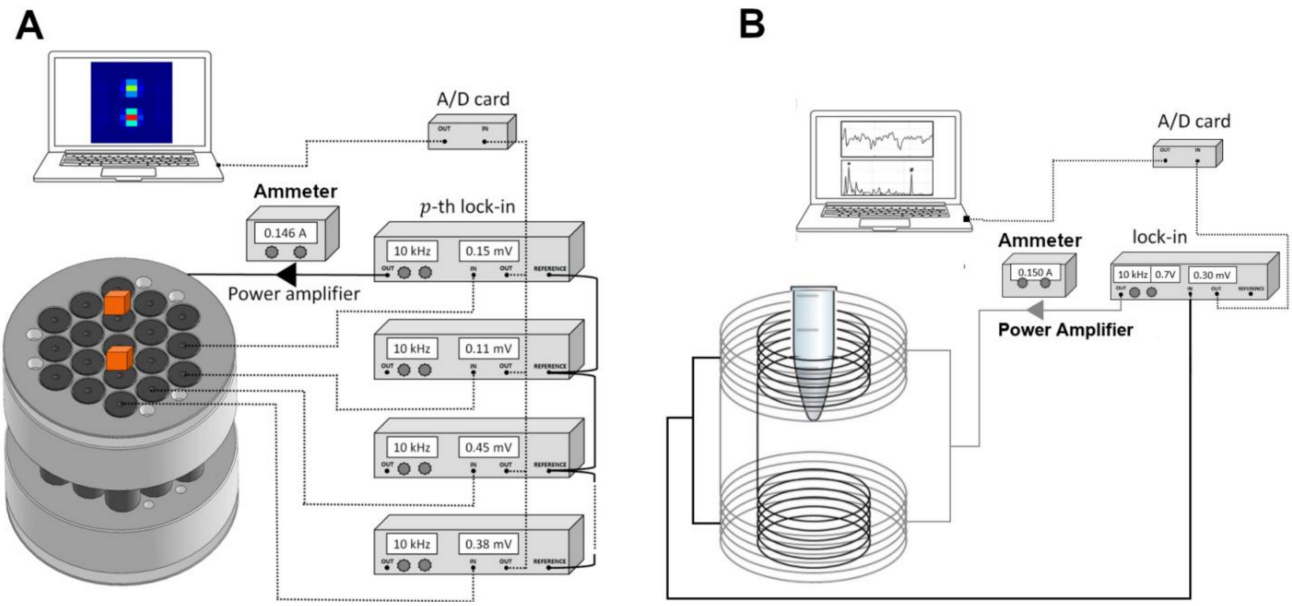

Figure 1. Schematic representation of both ABC setups utilized. (**A**) MC-ACB and (**B**) cavity ACB sensor.

2.3. Experimental Design of Cirrhosis-Associated Hepatocarcinogenesis Model

The current cirrhosis-associated hepatocarcinogenesis model was based on a previously published protocol [11]. In this rodent study, 36 males (*Rattus norvegicus albinus*, Wistar, weighing 250–300 g) provided by the UNESP animal facility (São Paulo State University) were divided into two groups. The animals were maintained under suitable conditions at 21 °C ± 1 °C with a 12 h/12 h light/dark cycle, constant air filtration, and ad libitum feeding. All animal experiments were previously approved and performed following the recommendations issued by the National Council for Control of Animal Experimentation (CONCEA) and were approved by the Ethics Committee on Animal Use of the São Paulo State University (IBB/UNESP) under protocol 7571041120.

The animals were randomly assigned to one of two groups, of which one was subjected to a NaCl 0.9% solution treatment (SAL-control group) and the other was subjected to the chemically-induced cirrhosis-associated hepatocarcinogenesis model (DEN/TAA group) [11].

The animals received a single intraperitoneal injection of diethylnitrosamine (DEN, 200 mg/kg in 0.9% saline solution) (Sigma-Aldrich, USA) to initiate liver carcinogenesis. After two weeks, we assigned the animals to three cycles of thioacetamide (TAA) (200 mg/kg in 0.9% saline solution) (Sigma-Aldrich, USA). During the fibrosis/cirrhosis induction, each TAA cycle was achieved after two intraperitoneal injections (twice a week), with an interval of one week without receiving treatment. The model of cirrhosis/hepatocarcinogenesis was carried out for eight weeks.

The animals were subjected to femoral vein cannulation surgery for the intravenous administration of MNPs (dose of 32 mg/kg) under anesthesia (99% urethane—1.5 mg/kg.) Then, the animals were positioned on the MC-ACB detection coils to carry out the magnetic in vivo biodistribution monitoring (further described in Section 2.4).

2.4. In Vivo Quantitative Imaging and Data Processing

We carried out quantitative MNP reconstruction by employing the MC-ACB, for which we had recently demonstrated the mathematical and computational approaches for improving the system's ability to acquire quantitative information [68]. We monitored the MNP biodistribution and recorded heart and liver signals using the MC-ACB system. We reconstructed the MNP biodistribution from the quantitative real-time signals, represented in sequential images (frames) at a sampling frequency of 20 Hz. Regions of interest (ROIs) were selected for the frames corresponding to the signals from the organs of interest

(liver and heart). We quantified a series of pharmacokinetic parameters from the MNP distribution signals of both organs over time.

2.5. Histopathological and Immunohistochemical Analysis

Liver tissue samples were washed, fixed in formalin, embedded in paraffin, and sequentially sectioned into 5 µm sections. Slides were stained with hematoxylin and eosin (H&E) and Sirius red (collagen deposition) for microscopic analysis. Other sections obtained on silane-coated slides (Starfrost, Lowestoft, UK) were subjected to immunohistochemical reactions to evaluate the expression of placental glutathione-S-transferase (GSTP) (i.e., preneoplastic and neoplastic marker) and CD68 (monocyte, macrophage, and Kupffer cell marker) antigens, as previously described [11,12].

The placental GST-P (π isoform) is expressed in initiated hepatocytes, but not in normal or non-initiated hepatocytes, indicating their role in hepatocarcinogenesis [71]. CD68 is a glycosylated type I transmembrane glycoprotein that is considered an important cytochemical marker for macrophages, especially in the histochemical analysis of inflamed tissues [72,73].

We performed a morphometric analysis (lesions and nodules positive for GST-P and collagen content) using the Leica Q-win Software, version 3.1. The H&E- and picro-Sirius-stained sections were analyzed under a Leica DMLB 80 microscope connected to a Leica DC300FX camera. After image digitalization, we measured each experimental liver area per group under 20× magnification in five fields. The fibrosis degree analysis was performed using the criteria reported previously [74].

2.6. Pharmacokinetic Study

To determine the pharmacokinetic profile of the Cit-$MnFe_2O_4$, we determined classical pharmacokinetic parameters that are commonly used, such as $T_{1/2}$ (half-life) and the area under the curve (AUC). We adapted the concept of drug exposure to the MNP bioavailability, which was calculated from the area under the liver curves of the two experimental groups. Regarding the liver signals, we quantified the highest MNP level detected (C_{Max}) and the time to the highest MNP level (T_{Max}).

Analysis of the Ex Vivo Biodistribution of the Cit-$MnFe_2O_4$

After the in vivo measurement to collect the quantitative information, the rodents from both groups (SAL and DEN/TAA) were euthanized at 60 min by decapitation after the MNP injection. Subsequently, the organs of interest, such as the liver, spleen, heart, lungs, and kidneys, were collected by a laparoscopy procedure. In this experimental procedure, we also collected a blood sample. To quantify and certify the mass of MNPs accumulated in each organ, we randomly picked a sample (100 mg) of each organ and the blood, which had been previously lyophilized, homogenized, and stored in a volume-controlled flask. According to the previous protocol, the samples were positioned on the ACB sensor for signal detection to determine the mass of MNPs using a calibration curve that was previously constructed from an MNP batch (initially 28 mg/mL) diluted into fourteen vials with different concentrations while controlling the volume. This procedure allowed for the comparison of the measured ACB signals to established MNP concentrations [42].

2.7. Statistical Analyses

Data were expressed as means ± standard deviations. An unpaired Student's *t*-test was used to compare the control and the treated groups' pharmacokinetic parameters ($T_{1/2}$, AUC, and biodistribution quantifications). The incidence data from the histological analysis were analyzed using Fisher's exact test. The other data were compared using the Mann–Whitney test or Student's *t*-test, considering a significance level of $p < 0.05$. Analyses were performed using GraphPad Prism 6.0 software (GraphPad, San Diego, CA, USA).

3. Results

3.1. MNP Characterization

We synthesized manganese ferrite nanoparticles coated with citrate (Cit-$MnFe_2O_4$) through the co-precipitation method. These MNPs were applied due to their excellent field magnetic response to the ACB system. At a concentration of 28 mg/mL, the MNPs showed a superparamagnetic behavior. According to our TEM results, they presented a core diameter of 24 ± 4 nm. Once the organic molecule citrate was small (from 1.5 to 10 nm), it was assumed that the MNP core indicated by the TEM images was equal to the diameter of the Cit-$MnFe_2O_4$ MNPs. Through the DLS Zetasizer results, the MNPs presented with a hydrodynamic size of 65.6 ± 4 nm, a polydispersion index for the colloid sample of 0.25, and a zeta potential of −27.8 mV. We observed a negative zeta potential for the magnetic Cit-$MnFe_2O_4$ (−27.8 ± 1.7 mV), which resulted from their surface being coated with citrate ions due to the effect of citrate adsorption onto bare MNPs. This value is in agreement with literature reports [69,74].

The assessment of magnetic characterization for the powder (pure MNPs) and colloidal solution (magnetic fluid) using an ADE Vibrating Sample Magnetometer (VSM) indicated a magnetization saturation of 52.8 emu/g. The magnetization profile showed a quasi-static superparamagnetic behavior (no coercive field at DC conditions) (see Figure 2C of [69]). We also confirmed the presence of Mn and Fe in the MNPs through an EDS analysis. The XRD analysis showed the structural characterization of the Cit-$MnFe_2O_4$ MNPs. The XRD pattern of as-dried $MnFe_2O_4$ confirmed the ferrite phase's formation. The diffraction peaks matched the single crystalline MnFe2O4 (JCPDS card No. 074–2403). The XRD results for $MnFe_2O_4$ were comparable with the previously reported results [75]. It is worth pointing out that we did not detect any impurity phases in the ferrite group. See Figure S5, Supplementary Materials. We confirmed the presence of the magnetic core and citrate shell through a Fourier-transform infrared (FTIR) analysis, observing bands at 1581 and 1383 cm^{-1} for the Cit-$MnFe_2O_4$ MNPs (black curve), which were assigned to the citrate due to the C-O bonds of the carboxylic group present in the molecule [76]. The absorption peak within 500–600 cm^{-1} corresponded to the Fe–O vibration, which was related to the magnetic phase [77]. All results of the MNP characterization process are described in the Supplementary Materials.

3.2. Macroscopic Aspects of Animals Subjected to Cirrhosis Associated with Hepatocarcinogenesis

Macroscopically, the livers from animals of the SAL group (Figure 2A) presented typical features (regular and smooth surfaces). On the other hand, the livers from animals of the DEN/TAA group (Figure 2B) presented rough surfaces with numerous nodules. These findings indicate that the animals subjected to the DEN/TAA protocol presented well-defined features of cirrhosis. In addition, as expected, the DEN/TAA treatment increased the animals' absolute and relative liver weight (RLW) (Figure 2C,D, respectively).

3.3. Histopathological Analysis, Collagen Morphometry, and Immunostaining

The histopathological analysis revealed that 80% (p = 0.049) and 20% of animals in the DEN/TAA group developed adenomas and HCC, respectively (Figure 3A). Compared to the SAL (control) group, the livers from the DEN/TAA group presented with multiple preneoplastic lesions and nodules that were positive for GSTP (Figure 3B, p = 0.0079). Sirius red-stained DEN/TAA liver sections demonstrated extensive collagen deposition (Figure 3C, p = 0.0079) with bridging fibrosis and cirrhotic nodules, and most were positive for GST-P (fibrosis level 5, p = 0.0079). Figure 3D shows the data for the immunohistochemical analysis of the CD68 marker. The results indicate that no statistical difference was observed in the macrophage counts between the SAL and DEN/TAA groups ($p > 0.05$).

3.4. Dynamic ACB Monitoring

We acquired images that dynamically represented the biodistribution of MNPs in real time through MC-ACB monitoring. The images were acquired sequentially, allowing for

a video representation of the circulation and accumulation processes. Figure 4 presents two frames showing moments of the MNP biodistribution for both experimental groups. In the first frame, at t = 820 s, an ROI was selected in the heart. The second frame, at t = 3600 s, corresponds to the liver region. These ROIs were applied to all the imaging frames, generating biodistribution curves. Previously, we positioned the animals on the MC-ACB system at the same projection to ensure the animal's anatomical references were kept during the biodistribution acquisition.

Consequently, Figure 4A shows the arrival of MNPs in the heart right after the MNP injection, while Figure 4B shows the final accumulation in the liver region. In order to demonstrate the difference between the MNP distributions, we quantified the average distribution of MNPs in the ROIs of the images. Figure 4C shows the MNPs in the bloodstream and liver. A high-intensity peak characterized the arrival of MNPs in the heart shortly after MNP injection. Then, the distribution of MNPs was represented by a rapid decay in the heart signal. Simultaneously, the liver captured and removed the MNPs from the bloodstream due to the high blood supply and many Kupffer cells in the hepatic tissue.

The liver signal can be associated with the uptake of macrophages and the accumulation of MNPs in the parenchyma. As depicted in Figure 4C (red curve), the liver showed a saturation tendency over time after a rapid intensity increase.

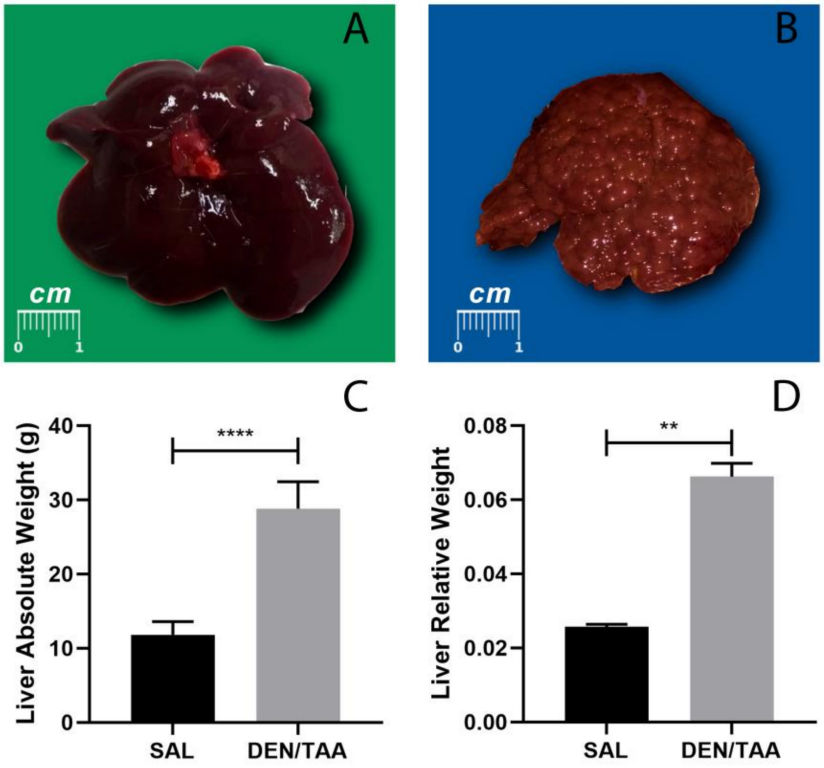

Figure 2. Representative images of macroscopic aspects of livers from (**A**) SAL-group animals and (**B**) DEN/TAA-group animals. Analyses of the absolute liver weight and relative liver weight are shown for (**C**) the SAL and (**D**) the DEN/TAA group. The relative liver weight (LW/BW) is expressed as the ratio between the liver weight (LW) and the body weight (BW). LW/BW ratio values are expressed as means ± sd; for the SAL and DEN/TAA groups, they were 0.25674 ± 0.000706 and 0.066253 ± 0.003554, respectively. (** $p < 0.05$) and (**** $p < 0.0001$).

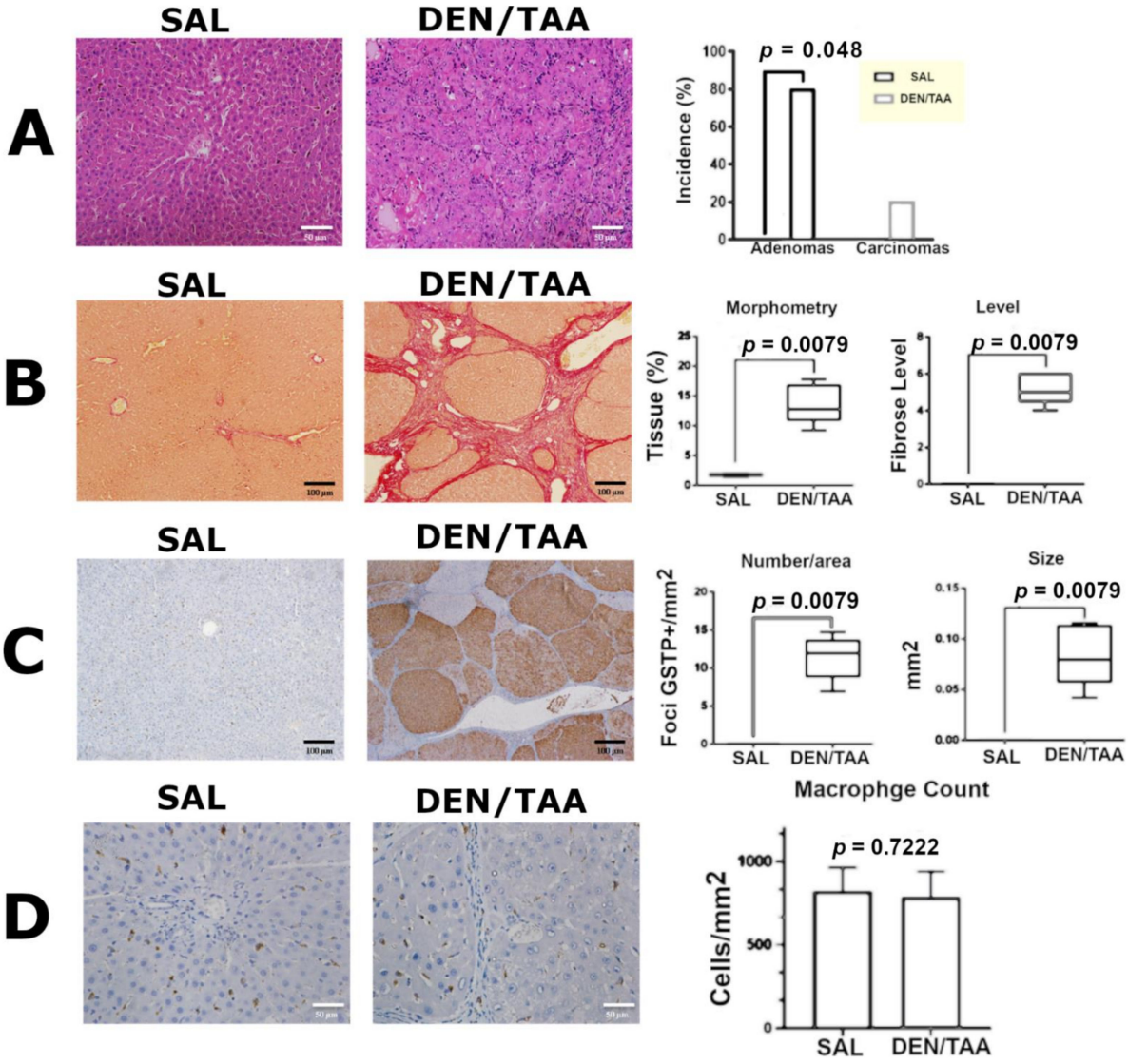

Figure 3. (**A**) Representative images of H&E-stained sections of SAL (left) and DEN/TAA (center) livers; HCC was characterized by profound cellular atypia and was composed of malignant hepatocytes arranged in acinar structures in the DEN/TAA group. Data on the incidence of adenomas and carcinomas are presented in terms of proportion (%) of affected animals and were analyzed by Fisher's exact test ($p < 0.05$) (right). (**B**) Collagen analysis shown with picro-Sirius red, showing sections from the SAL (left) and DEN/TAA (center) groups. Morphometry and degree of fibrosis data are presented in box plots and were analyzed using the Mann–Whitney test ($p < 0.05$) (right). (**C**) Immunohistochemistry sections from the SAL group (left) and the multiple GST-P+ nodules in the DEN/TAA group (center). The number and size of GST-P+ lesions are presented in box plots and were analyzed using the Mann–Whitney test ($p < 0.05$) (right). (**D**) Immunohistochemistry for the CD68 marker in sections from the SAL (left) and DEN/TAA (center) groups, showing macrophages. Macrophage count data are presented as means and standard deviations and were analyzed using a *t*-test ($p < 0.05$) (right).

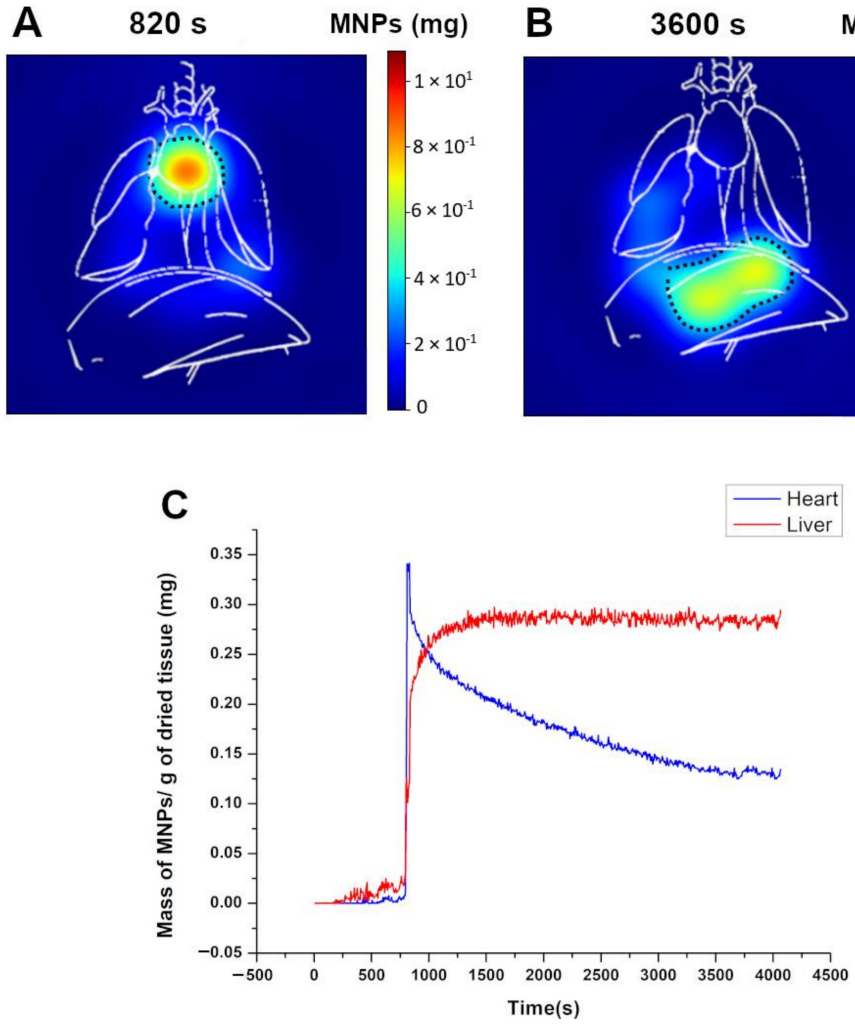

Figure 4. Representation of the biodistribution by frames after injection and the specific ROIs selected to access the pharmacokinetic parameters; (**A**) 820 s, showing the high and low concentrations of MNPs in the heart and the liver, respectively; (**B**) 3600 s, indicating the final biodistribution process, which was characterized by a solely higher intensity signal in the liver; and (**C**) the average intensity over time for ROI 1 (heart region) and ROI 2 (liver).

3.5. Pharmacokinetic Assessment and MNP Biodistribution

The kinetics of MNP accumulation were evaluated to prove the liver performance during MNP uptake. The kinetics of MNP accumulation were assessed by plotting graphs of the liver signals previously obtained from ROI imaging. To determine the liver's accumulation, we employed the classical concept of the AUC. We found a significant difference ($p < 0.0001$) between the rates of MNP deposition in the hepatic tissue of the animal groups. The pharmacokinetic assessment of hepatic curves also indicated significant differences ($p < 0.0001$) in C_{max} and T_{max} for the DEN/TAA group. The evaluation of liver signals revealed that the healthy livers reached C_{max} after 26.63 min (T_{max}).

On the other hand, the livers under a cirrhosis-induced process had an inversed profile, presenting with a lower peak concentration that was reached in a shorter time (T_{max} of 16.7 min) and remained constant over time. Through the plotted heart curves, we assessed the $T_{1/2}$ of the MNPs. The exponential decay analyses of the DEN/TAA group showed a half-life of 16.3 min compared to 28.3 min for the SAL group. All the pharmacokinetic parameters of the DEN/TAA group were found to be significantly different from the SAL group (Student *t*-test, $p < 0.05$). The pharmacokinetic parameters are summarized in Table 1.

Table 1. Pharmacokinetic parameters of Cit-$MnFe_2O_4$ MNPs after intravenous administration at a 32 mg/kg dose for the SAL and DEN/TAA groups. C_{max} = the highest MNP level detected; T_{max} = the time to the highest MNP level; AUC = the area under the curve; $T_{1/2}$ = half-life. **** $p < 0.0001$.

Pharmacokinetic Parameter	Evaluation (Mean ± SD)	
	SAL	DEN/TAA
C_{max} (mg MNP/dose injected)	0.4870 ± 0.01212	0.4150 ± 0.01621 ****
T_{max} (m)	26.63 ± 0.5145	16.71 ± 1.1 ****
$AUC_{0–60min}$	1472.6 ± 201	1198.5 ± 152 ****
$T_{1/2}$ (min)	19.6 ± 2.3	11.2 ± 3.1 ****

After acquiring the signals from the in vivo biodistribution measurements and the euthanasia of the animals, we started the protocol to analyze the ex vivo biodistribution from the collected organs as described in Analysis of the Ex Vivo Biodistribution of the Cit-$MnFe_2O_4$ section. From our system's ACB characterization, we found a limit of detection (LOD) of 12 μg and a limit of quantification (LOQ) of 40 μg for the MNP reference. The sensitivity was 0.9 (χ/mg (MNPs). Figure 5 presents the profile for the ex vivo MNP biodistribution. In general, we noticed a similar behavior of the MNP biodistribution between the experimental groups, where the spleen retained most of the particles, followed by the liver and lungs. However, we found significant differences between the control and treated groups for the same organs (spleen, liver, and lungs), indicating a higher accumulation for the SAL group. The ACB quantification revealed that the MNP accumulation in organs such as the heart and kidneys was minimal, with these organs presenting with very low values of MNP deposition. Both organs do not typically specialize in MNP retention and capture, which would explain the low signal. In addition, the two organs did not show significant differences between the groups, suggesting that besides the MNP properties, which would facilitate the splenic and hepatic uptake, the induced liver injury could not influence MNP deposition in these organs.

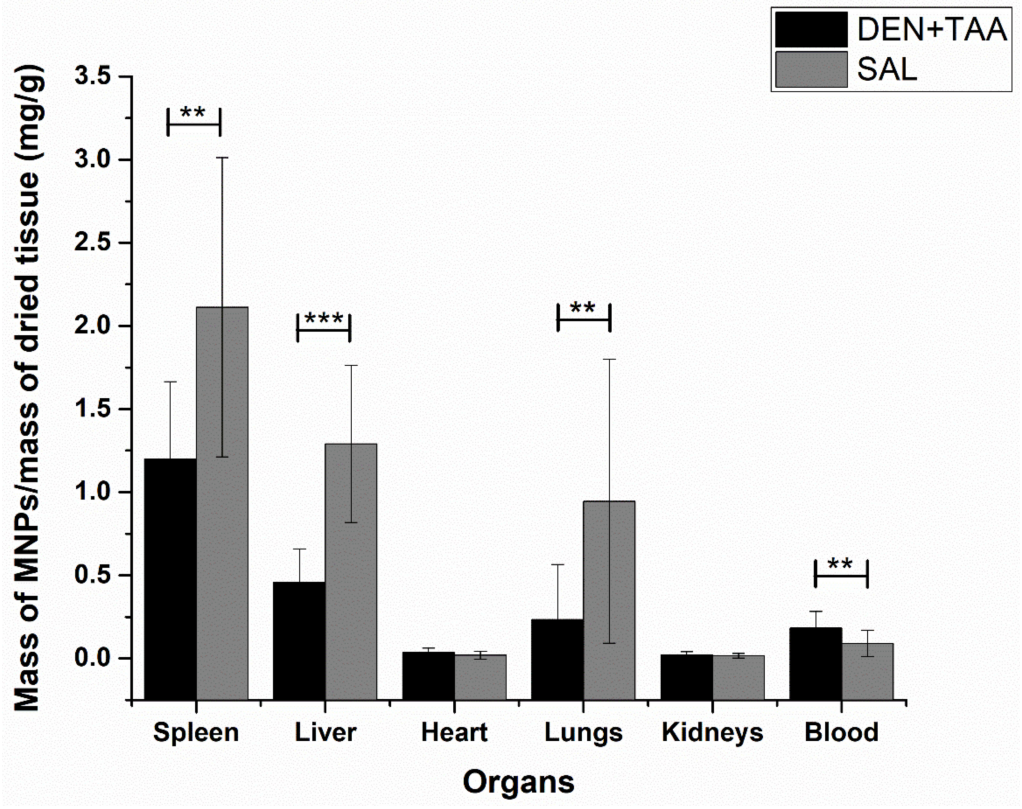

Figure 5. ACB data for MNP biodistribution in SAL and DEN/TAA; ** $p < 0.05$; *** $p < 0.01$.

The biodistribution analysis also indicated differences in the MNPs found in the blood samples. At the end of 60 min, the amounts of MNPs found in the SAL group's spleen, liver, and lungs were significantly higher than those in the DEN/TAA group.

4. Discussion

Besides its properties such as an excellent low-field magnetic response and a high magnetization saturation, Cit-$MnFe_2O_4$ presents with a negative zeta potential. According to the literature, nanomaterials with positive zeta potentials show an increased clearance [78–81]. It is generally known that positively charged nanoparticles have faster blood clearance, while neutral and negative particles exhibit a longer circulation time [82–85]. In addition, nanoparticles with a negative charge present with a lower Kupffer cell uptake in addition to their higher circulation time, which contributes to an increased tumor uptake [86,87]. Furthermore, a strongly negative potential allows the particles to be stable over a variety of pH levels and effectively prevents agglomeration due to steric and electrostatic forces from the citrate layer. The MNPs employed in this study were selected due to their ability to act exclusively as tracers for in vivo measurements, as the aim of this work was to assess liver cirrhosis under the MC-ACB system. Therefore, manganese ferrite nanoparticles are not functionalized with biotherapeutics and chemotherapeutics to work as cirrhosis treatment vehicles based on drug delivery systems and gene therapy.

Although there have been numerous alternatives to the treatment of chronic liver diseases such as cirrhosis and HCC, limitations such as non-specific targeting and adequate drug delivery concentrations have reduced the chances for the successful treatment of these illnesses. Therefore, new agents with improved therapeutic efficiencies have been investigated. However, new translational studies assessing the pathophysiological and pharmacokinetic profiles in liver cirrhosis are essential, as they will contribute to new perspectives in the approach and investigation of new drugs.

In the present study, we assessed the biodistribution profile of MNPs in a rat cirrhotic microenvironment associated with hepatocarcinogenesis, in which a complete assessment performed by the ACB system—which included real-time monitoring and the quantification of the accumulation of MNPs—was evaluated. It is noteworthy that the Cit-$MnFe_2O_4$ used here exhibited great potential for the diagnosis and study of hepatic diseases such as cirrhosis, as previously reported [33]. In addition, this magnetic particle system can be used as an efficient agent in magnetic hyperthermia due to its unique properties [88]. Thus, our real-time in vivo study was performed through image acquisition or distribution profiling of intravenously administered MNPs. The same system was employed to assess the biodistribution process in normal and injured livers in a DEN/TAA protocol.

The different ACB analyses allowed for a complete pharmacokinetic assessment, confirming that the spleen and the liver are the primary organs responsible for capturing MNPs after intravenous injection. The higher retention of MNPs in the spleen and liver can be attributed to the role of the MPS. According to several reports, most injected MNPs are cleared from the bloodstream by specialized cells, such as the resident macrophages of the liver (Kupffer cells) and spleen (red pulp macrophages) [89,90].

The in vivo results were confirmed by an ex vivo biodistribution analysis (spleen, liver, and lungs), indicating that in the DEN/TAA group, a lower uptake of MNPs occurred compared to that in healthy animals. The spleen plays a significant role in the clearance of MNPs from the bloodstream. Due to its close anatomic proximity to the liver, a communication axis between the liver and spleen ("liver–spleen axis") is commonly reported [91,92]. Furthermore, in the course of cirrhosis with portal hypertension, the spleen volume undergoes an increase in volume that is proportional to the degree of damage to the liver function [4,93]. However, the mechanisms underlying the splenic function under cirrhosis remain unknown. In a study that addressed liver cirrhosis, the authors found a decreased MNP accumulation in the liver. In contrast, the spleen under cirrhosis showed a higher uptake than in non-cirrhotic animals [94]. Despite the spleen's phagocytic activity increasing with splenomegaly [95], another study indicated that the hepatic uptake of nanocarriers is

affected by liver disease, whereas the splenic uptake was partially affected [96]. In addition, another work also found that patients with liver cirrhosis presented with a decreased liver and spleen uptake of a superparamagnetic contrast agent for magnetic resonance imaging [97].

In this way, we believe that liver cirrhosis possibly induces a decreased uptake of the red zone macrophages in the spleen. It is worth pointing out that the red pulp is constituted by the macrophage population, which retains much of the administered nanoparticles.

Firstly, we also hypothesized that the DEN/TAA-induced protocol could have led to an abrupt depletion of the KCs, which is supported by several studies after toxic hepatic injury and infections [98,99]. However, our immunohistochemistry findings with the CD68 marker indicated no statistical differences in the counts of infiltrated macrophages and resident Kupffer cells between the SAL and DEN/TAA groups. It is worth pointing out that the depletion of KCs is not a mechanism related to all types of liver damage. For example, Kessler et al. [100] performed a DEN treatment to induce severe liver damage and did not find a significant KC loss in the short-term or long-term DEN models.

Concerning the accumulation by the liver, the IV administration of MNPs can reach the hepatocytes. The hepatocytes represent 70% of total liver cells and are separated from the sinusoids by the space of Disse [101]. As mentioned above, hepatic sinusoids are constituted by endothelial cells that have a fenestrated cytoplasm associated with a discontinuous basal lamina [101]. Through their fenestrae, the LSECs allow absorption and secretion to take place across the narrow space of Disse, creating a unique channel for blood–hepatocyte exchange across sinusoids [102]. In addition to being highly porous, hepatic sinusoids are characterized by the absence of an organized basal lamina in healthy conditions.

Nevertheless, hepatic disturbances and diseases such as fibrosis and cirrhosis induce a capillarization process in the LSECs, which leads to the loss of their fenestrated characteristics [103,104]. A continuous basal lamina characterizes the process of capillarization in hepatic sinusoids, thus avoiding the bidirectional traffic of molecules in the blood and the parenchyma, and vice versa [105,106]. Therefore, this could be considered the main reason for the change in the MNP biodistribution.

By comparing our data for MNP accumulation in the livers of the DEN/TAA group, the results suggest that the increases in intrahepatic vascular resistance, impaired hepatic sinusoidal circulation, collagen deposition, and portal hypertension, which are associated with cirrhosis [107], could influence the arrival of MNPs to the liver. When we analyzed the data for MNP accumulation in the DEN/TAA and SAL groups, the liver presented with a higher significant *p*-value, followed by the spleen and the lungs. We noticed a lower MNP accumulation in the DEN/TAA group, suggesting a decreased hepatic uptake and consequently more MNPs circulating, which was visualized through the statistical differences in the blood analyses (Figure 5). During the liver cirrhosis process, the hepatic tissue undergoes chronic damage and an inflammatory process, during which a repair process is initiated to regenerate damaged hepatocytes, resulting in scar formation. Therefore, we also assumed that besides the capillarization process, there is a loss of hepatocytes in the fibrosis state by connective tissue scars, which could affect MNP uptake, since an altered obstruction of blood circulation with portal hypertension can occur in this chronic disease [108].

Besides liver disorders, chronic liver disease can result in pulmonary complications. In this way, hepatopulmonary syndrome (HPS) is commonly associated with cirrhosis [109]. HPS is a pulmonary disorder characterized by arterial oxygen desaturation, pulmonary vascular vasodilation, and intrapulmonary shunts. The increased shunting associated with pulmonary vasodilatation is responsible for the imbalance between perfusion and ventilation, causing abnormalities in gas exchange [110,111]. This compromised lung profile could explain the lung biodistribution results for the DEN/TAA group, in which the MNPs did not reach the lung alveoli, and consequently did not remain in the tissue.

The pharmacokinetic assessment results confirmed that the DEN and TAA administration model caused damage that altered the liver architecture. Besides the biodistribution results, we noticed that the livers from the DEN/TAA group presented with a limited uptake efficiency of MNP, as observed by the C_{max}. We assumed that the altered basal lamina in hepatic sinusoids did not allow blood extravasation towards hepatocytes. In this way, we hypothesized that the new basal lamina in hepatic sinusoids affected the interaction between the blood and the hepatocytes in the DEN/TAA group. In contrast to the control group, the DEN/TAA protocol resulted in an altered blood flow in hepatocytes, which might have decreased liver uptake. Consequently, the non-extravasation towards hepatocytes resulted in early Kupffer cell saturation, according to our values for T_{max}. Despite the fact that hepatocytes are not specialized to retain MNPs, the possible deposition in the hepatocytes might be attributed to the diameter of the Cit-$MnFe_2O_4$ MNPs, which was smaller than the fenestrations of the sinusoids [112]. We noticed that the livers under cirrhosis took less time to exhibit a saturation profile, while the healthy livers continued the exchange between the hepatocytes and the hepatic sinusoidal blood. Therefore, we also assumed that a part of the injected MNPs penetrated the sinusoid and reached the hepatocytes in the SAL group. This condition would explain the significant differences in the observed pharmacokinetic profiles, such as the MNP accumulation.

Since our biodistribution results (Figure 5) indicated a lower hepatic uptake for the DEN/TAA group, it instantly led us to consider a longer circulation time of MNPs for this group. As depicted in Figure 2C,D, the DEN/TAA animals presented with an increased liver weight compared to the SAL group. However, to assess the biodistribution profile, we employed a protocol to calculate the mass of particles per gram of lyophilized tissue. The hepatic uptake of DEN/TAA would be higher due to its mass in a quantification using absolute values. It was evident by the non-normalized $T_{1/2}$ values that the livers under these conditions influenced the circulation time of MNPs.

Although the MC-ACB presented a high temporal resolution for acquiring the biodistribution of MNPs dynamically, but only for the liver and heart, we believe that an improvement mainly in the coil array might lead the system to detect the MNP biodistribution in other target organs.

This study reported an application of a new and improved MC-ACB system compared to the previous one [48], where the main progress was the acquisition of quantitative in vivo images of the MNP distribution in healthy and neoplastic animals.

In this context, we believe this methodology is adequate for investigating several organs and their functions, either in normal circumstances or while under dysfunction.

Nevertheless, nanotechnology-based magnetic systems are an alternative strategy to the conventional methods for the investigation of liver diseases. These systems can perform non-invasive imaging assessments to work towards an early diagnosis, which might contribute to the efficient delivery of therapeutics to the liver.

5. Conclusions

As highlighted by the presented findings, the pharmacokinetic profile of MNP distribution and accumulation was affected by pathophysiological factors induced by a cirrhosis state. Since the liver monocytes and macrophages remained stable, the differences found in the pharmacokinetic profile of cirrhotic animals strongly indicate that hepatic blood flow is most likely responsible for altering the distribution and accumulation profile of MNPs. Therefore, the feasibility of developing nanotechnology-based delivery platforms needs further investigation to address strategies to improve the interaction of therapeutic agents with injured hepatic tissue.

Through an in vivo and ex vivo information acquisition approach, the ACB system provided the ability to monitor and quantify the MNPs in healthy and cirrhosis conditions, providing the requirements necessary to assist in the diagnosis and therapy of hepatic disorders. By extrapolating the possibilities of evaluation to problems found in the clinical environment, the association of the ACB system with MNPs might offer a methodology

with easy access, a low cost, and the absence of ionizing radiation to assess several biologic functions under disorders. Furthermore, it is expected that through instrumental improvements, the MC-ACB system will be enhanced to the level of relevant methodologies such as magnetic particle imaging and magnetorelaxometry.

Supplementary Materials: The following supporting information can be downloaded at: https://www.mdpi.com/article/10.3390/pharmaceutics14091907/s1, Figure S1: (A) Image of MNPs at 100 nm scale. (B) Image of MNPs at 50 nm scale. Figure S2: Hydrodynamic size obtained by the dynamic light scattering experiment. Figure S3: (A) Magnetization curve of MNPs in a fluid sample and a powder sample (B) acquired by the VSM experiment. Figure S4: EDS quantification of the MNPs composition quantification. (A) MNPs sample used, in which the numbers (1, 2, and 3) represent the studied region. (B) Representative example of EDS signal acquired and its quantification (region 2 of the MNPs image). Figure S5. X-ray diffractogram of Cit-$MnFe_2O_4$ MNPs. Figure S6: FTIR measurements of citrate and the Cit-$MnFe_2O_4$ MNPs.

Author Contributions: Conceptualization, G.A.S., G.R.R., L.F.B., and J.R.A.M.; methodology, L.F.B., J.R.A.M., and G.A.S.; software, G.G.A.B., G.R.R., and G.M.P.; validation, G.G.A.B., E.G.S., and G.R.R.; formal analysis, G.A.S., G.G.A.B., G.R.R., G.M.P., E.G.S., and J.R.A.M.; investigation, G.M.P. and G.A.S.; resources, G.A.S., G.M.P., and G.R.R.; data acquisition, G.A.S., G.M.P., E.G.S. and G.G.A.B.; writing—original draft preparation, G.A.S., O.B., E.G.S., G.M.P., and G.G.A.B.; writing—review and editing, G.A.S., A.F.B., G.R.R., L.F.B., and J.R.A.M.; supervision, O.B., A.F.B., J.R.A.M., G.R.R., and L.F.B.; project administration, O.B., A.F.B., and J.R.A.M.; funding acquisition, O.B., J.R.A.M., L.F.B., and A.F.B. All authors have read and agreed to the published version of the manuscript.

Funding: This work was supported by the Fundação de Amparo à Pesquisa do Estado de São Paulo (FAPESP), grants 2013/07699-0, 2021/06405-9, 2021/09829-4 and 2019/11277-0. It was also supported by the Conselho Nacional de Pesquisas e Desenvolvimento Tecnológico (CNPq), grants 312074/2018-9 and 311074/2018. The German Academic Exchange program DAAD in cooperation with Brazilian CAPES-PROBRAL (project ID 57446914, 88887.198747/2018-00, and 888 81.198748/2018-01) supported this work.

Institutional Review Board Statement: The study was conducted and approved by the São Paulo State University (UNESP) Committee for the Use and Care of Animals (protocol No. CEUA—IBB 7571041120).

Informed Consent Statement: Not applicable.

Data Availability Statement: Almost all data are presented within the manuscript (figures and tables). The raw data presented in this study are available upon request to the corresponding author.

Acknowledgments: We would like to thank Mirella Visnosvescki Fogaca for the support in the ex vivo measurements.

Conflicts of Interest: The authors declare no conflict of interest.

References

1. Malarkey, D.E.; Johnson, K.; Ryan, L.; Boorman, G.; Maronpot, R.R. New insights into functional aspects of liver morphology. *Toxicol. Pathol.* **2005**, *33*, 27–34. [CrossRef] [PubMed]
2. Binatti, E.; Gerussi, A.; Barisani, D.; Invernizzi, P. The Role of Macrophages in Liver Fibrosis: New Therapeutic Opportunities. *Int. J. Mol. Sci.* **2022**, *23*, 6649. [CrossRef] [PubMed]
3. Nianan, L.; Jiangbin, L.; Yu, W.; Jianguo, L.; Rui, D. Hepatic Stellate Cell: A Double-Edged Sword in the Liver. *Physiol. Res.* **2021**, *70*, 821.
4. Ezhilarasan, D. Advantages and challenges in nanomedicines for chronic liver diseases: A hepatologist's perspectives. *Eur. J. Pharmacol.* **2021**, *893*, 173832. [CrossRef]
5. Desmet, V.J.; Roskams, T. Cirrhosis reversal: A duel between dogma and myth. *J. Hepatol.* **2004**, *40*, 860–867. [CrossRef]
6. Hoekstra, L.T.; de Graaf, W.; Nibourg, G.A.; Heger, M.; Bennink, R.J.; Stieger, B.; van Gulik, T.M. Physiological and biochemical basis of clinical liver function tests: A review. *Ann. Surg.* **2013**, *257*, 27–36. [CrossRef]
7. Sung, H.; Ferlay, J.; Siegel, R.L.; Laversanne, M.; Soerjomataram, I.; Jemal, A.; Bray, F. Global cancer statistics 2020: GLOBOCAN estimates of incidence and mortality worldwide for 36 cancers in 185 countries. *CA A Cancer J. Clin.* **2021**, *71*, 209–249. [CrossRef]
8. Yang, J.D.; Kim, W.R.; Coelho, R.; Mettler, T.A.; Benson, J.T.; Sanderson, S.O.; Therneau, T.M.; Kim, B.; Roberts, L.R. Cirrhosis is present in most patients with hepatitis B and hepatocellular carcinoma. *Clin. Gastroenterol. Hepatol.* **2011**, *9*, 64–70. [CrossRef]

9. Greten, T.; Papendorf, F.; Bleck, J.; Kirchhoff, T.; Wohlberedt, T.; Kubicka, S.; Klempnauer, J.; Galanski, M.; Manns, M. Survival rate in patients with hepatocellular carcinoma: A retrospective analysis of 389 patients. *Br. J. Cancer* **2005**, *92*, 1862–1868. [CrossRef]
10. Op den Winkel, M.; Nagel, D.; Sappl, J.; op den Winkel, P.; Lamerz, R.; Zech, C.J.; Straub, G.; Nickel, T.; Rentsch, M.; Stieber, P. Prognosis of patients with hepatocellular carcinoma. Validation and ranking of established staging-systems in a large western HCC-cohort. *PLoS ONE* **2012**, *7*, e4506.
11. Romualdo, G.R.; Grassi, T.F.; Goto, R.L.; Tablas, M.B.; Bidinotto, L.T.; Fernandes, A.A.H.; Cogliati, B.; Barbisan, L.F. An integrative analysis of chemically-induced cirrhosis-associated hepatocarcinogenesis: Histological, biochemical and molecular features. *Toxicol. Lett.* **2017**, *281*, 84–94. [CrossRef]
12. Romualdo, G.R.; Prata, G.B.; da Silva, T.C.; Fernandes, A.A.H.; Moreno, F.S.; Cogliati, B.; Barbisan, L.F. Fibrosis-associated hepatocarcinogenesis revisited: Establishing standard medium-term chemically-induced male and female models. *PLoS ONE* **2018**, *13*, e0203879. [CrossRef]
13. Romualdo, G.R.; Leroy, K.; Costa, C.J.S.; Prata, G.B.; Vanderborght, B.; Da Silva, T.C.; Barbisan, L.F.; Andraus, W.; Devisscher, L.; Câmara, N.O.S. In vivo and in vitro models of hepatocellular carcinoma: Current strategies for translational modeling. *Cancers* **2021**, *13*, 5583. [CrossRef]
14. Salarian, M.; Turaga, R.C.; Xue, S.; Nezafati, M.; Hekmatyar, K.; Qiao, J.; Zhang, Y.; Tan, S.; Ibhagui, O.Y.; Hai, Y.; et al. Early detection and staging of chronic liver diseases with a protein MRI contrast agent. *Nat. Commun.* **2019**, *10*, 4777. [CrossRef]
15. Li, C.; Li, R.; Zhang, W. Progress in non-invasive detection of liver fibrosis. *Cancer Biol. Med.* **2018**, *15*, 124–136. [CrossRef]
16. Surendran, S.P.; Thomas, R.G.; Moon, M.J.; Jeong, Y.Y. Nanoparticles for the treatment of liver fibrosis. *Int. J. Nanomed.* **2017**, *12*, 6997. [CrossRef]
17. Sumida, Y.; Nakajima, A.; Itoh, Y. Limitations of liver biopsy and non-invasive diagnostic tests for the diagnosis of nonalcoholic fatty liver disease/nonalcoholic steatohepatitis. *World J. Gastroenterol.* **2014**, *20*, 475–485. [CrossRef]
18. Cheng, Z.; Lv, Y.; Pang, S.; Bai, R.; Wang, M.; Lin, S.; Xu, T.; Spalding, D.; Habib, N.; Xu, R. Kallistatin, a new and reliable biomarker for the diagnosis of liver cirrhosis. *Acta Pharm. Sin. B* **2015**, *5*, 194–200. [CrossRef]
19. Lin, Y.-S. Ultrasound Evaluation of Liver Fibrosis. *J. Med. Ultrasound* **2017**, *25*, 127–129. [CrossRef]
20. Petitclerc, L.; Gilbert, G.; Nguyen, B.N.; Tang, A. Liver Fibrosis Quantification by Magnetic Resonance Imaging. *Top Magn. Reson. Imaging* **2017**, *26*, 229–241. [CrossRef]
21. Huber, A.; Ebner, L.; Heverhagen, J.T.; Christe, A. State-of-the-art imaging of liver fibrosis and cirrhosis: A comprehensive review of current applications and future perspectives. *Eur. J. Radiol. Open* **2015**, *2*, 90–100. [CrossRef] [PubMed]
22. Salarian, M.; Ibhagui, O.Y.; Yang, J.J. Molecular imaging of extracellular matrix proteins with targeted probes using magnetic resonance imaging. *Wiley Interdiscip. Rev. Nanomed. Nanobiotechnol.* **2020**, *12*, e1622. [CrossRef] [PubMed]
23. Reddy, L.H.; Couvreur, P. Nanotechnology for therapy and imaging of liver diseases. *J. Hepatol.* **2011**, *55*, 1461–1466. [CrossRef] [PubMed]
24. Bai, X.; Su, G.; Zhai, S. Recent advances in nanomedicine for the diagnosis and therapy of liver fibrosis. *Nanomaterials* **2020**, *10*, 1945. [CrossRef]
25. Jin, Y.; Wang, H.; Yi, K.; Lv, S.; Hu, H.; Li, M.; Tao, Y. Applications of Nanobiomaterials in the Therapy and Imaging of Acute Liver Failure. *Nano-Micro Lett.* **2020**, *13*, 25. [CrossRef]
26. Liu, Q.; Song, L.; Chen, S.; Gao, J.; Zhao, P.; Du, J. A superparamagnetic polymersome with extremely high T2 relaxivity for MRI and cancer-targeted drug delivery. *Biomaterials* **2017**, *114*, 23–33. [CrossRef]
27. Patra, J.K.; Das, G.; Fraceto, L.F.; Campos, E.V.R.; Rodriguez-Torres, M.d.P.; Acosta-Torres, L.S.; Diaz-Torres, L.A.; Grillo, R.; Swamy, M.K.; Sharma, S.; et al. Nano based drug delivery systems: Recent developments and future prospects. *J. Nanobiotechnol.* **2018**, *16*, 71. [CrossRef]
28. Yao, Y.; Zhou, Y.; Liu, L.; Xu, Y.; Chen, Q.; Wang, Y.; Wu, S.; Deng, Y.; Zhang, J.; Shao, A. Nanoparticle-Based Drug Delivery in Cancer Therapy and Its Role in Overcoming Drug Resistance. *Front. Mol. Biosci.* **2020**, *7*, 193. [CrossRef]
29. Yu, Z.; Gao, L.; Chen, K.; Zhang, W.; Zhang, Q.; Li, Q.; Hu, K. Nanoparticles: A New Approach to Upgrade Cancer Diagnosis and Treatment. *Nanoscale Res. Lett.* **2021**, *16*, 88. [CrossRef] [PubMed]
30. Talaei, S.; Mellatyar, H.; Pilehvar-Soltanahmadi, Y.; Asadi, A.; Akbarzadeh, A.; Zarghami, N. 17-Allylamino-17-demethoxygeldanamycin loaded PCL/PEG nanofibrous scaffold for effective growth inhibition of T47D breast cancer cells. *J. Drug Deliv. Sci. Technol.* **2019**, *49*, 162–168. [CrossRef]
31. Ahlawat, J.; Hooda, R.; Sharma, M.; Kalra, V.; Rana, J.; Batra, B. Nanoparticles in Biomedical Applications. In *Green Nanoparticles*; Springer: Cham, Switzerland, 2020; pp. 227–250.
32. Li, Y.; Shang, W.; Liang, X.; Zeng, C.; Liu, M.; Wang, S.; Li, H.; Tian, J. The diagnosis of hepatic fibrosis by magnetic resonance and near-infrared imaging using dual-modality nanoparticles. *RSC Adv.* **2018**, *8*, 6699–6708. [CrossRef] [PubMed]
33. Saraswathy, A.; Nazeer, S.S.; Nimi, N.; Santhakumar, H.; Suma, P.R.; Jibin, K.; Victor, M.; Fernandez, F.B.; Arumugam, S.; Shenoy, S.J.; et al. Asialoglycoprotein receptor targeted optical and magnetic resonance imaging and therapy of liver fibrosis using pullulan stabilized multi-functional iron oxide nanoprobe. *Sci. Rep.* **2021**, *11*, 18324. [CrossRef] [PubMed]
34. Nagórniewicz, B.; Mardhian, D.F.; Booijink, R.; Storm, G.; Prakash, J.; Bansal, R. Engineered Relaxin as theranostic nanomedicine to diagnose and ameliorate liver cirrhosis. *Nanomed. Nanotechnol. Biol. Med.* **2019**, *17*, 106–118. [CrossRef]
35. Ezhilararasan, D.; Lakshmi, T.; Raut, B. Novel Nano-Based Drug Delivery Systems Targeting Hepatic Stellate Cells in the Fibrotic Liver. *J. Nanomater.* **2021**, *2021*, 4674046. [CrossRef]

36. Eslaminejad, T.; Noureddin Nematollahi-Mahani, S.; Ansari, M. Glioblastoma targeted gene therapy based on pEGFP/p53-loaded superparamagnetic iron oxide nanoparticles. *Curr. Gene Ther.* **2017**, *17*, 59–69. [CrossRef]
37. Li, F.; Yan, H.; Wang, J.; Li, C.; Wu, J.; Wu, S.; Rao, S.; Gao, X.; Jin, Q. Non-invasively differentiating extent of liver fibrosis by visualizing hepatic integrin αvβ3 expression with an MRI modality in mice. *Biomaterials* **2016**, *102*, 162–174. [CrossRef]
38. Ungureanu, B.S.; Teodorescu, C.M.; Saftoiu, A. Magnetic Nanoparticles for Hepatocellular Carcinoma Diagnosis and Therapy. *J. Gastrointest. Liver Dis. JGLD* **2016**, *25*, 375–383. [CrossRef]
39. Hume, D.A. Differentiation and heterogeneity in the mononuclear phagocyte system. *Mucosal Immunol.* **2008**, *1*, 432–441. [CrossRef]
40. Alexis, F.; Pridgen, E.; Molnar, L.K.; Farokhzad, O.C. Factors affecting the clearance and biodistribution of polymeric nanoparticles. *Mol. Pharm.* **2008**, *5*, 505–515. [CrossRef]
41. Colino, C.I.; Lanao, J.M.; Gutierrez-Millan, C. Targeting of hepatic macrophages by therapeutic nanoparticles. *Front. Immunol.* **2020**, *11*, 218. [CrossRef]
42. Próspero, A.G.; Soares, G.A.; Moretto, G.M.; Quini, C.C.; Bakuzis, A.F.; de Arruda Miranda, J.R. Dynamic cerebral perfusion parameters and magnetic nanoparticle accumulation assessed by AC biosusceptometry. *Biomed. Eng./Biomed. Tech.* **2020**, *65*, 343–351. [CrossRef]
43. Próspero, A.G.; Quini, C.C.; Bakuzis, A.F.; Fidelis-de-Oliveira, P.; Moretto, G.M.; Mello, F.P.; Calabresi, M.F.; Matos, R.V.; Zandoná, E.A.; Zufelato, N. Real-time in vivo monitoring of magnetic nanoparticles in the bloodstream by AC biosusceptometry. *J. Nanobiotechnol.* **2017**, *15*, 22. [CrossRef] [PubMed]
44. Zhang, H.; Li, L.; Liu, X.L.; Jiao, J.; Ng, C.-T.; Yi, J.B.; Luo, Y.E.; Bay, B.-H.; Zhao, L.Y.; Peng, M.L.; et al. Ultrasmall Ferrite Nanoparticles Synthesized via Dynamic Simultaneous Thermal Decomposition for High-Performance and Multifunctional T1 Magnetic Resonance Imaging Contrast Agent. *ACS Nano* **2017**, *11*, 3614–3631. [CrossRef]
45. Park, J.Y.; Daksha, P.; Lee, G.H.; Woo, S.; Chang, Y. Highly water-dispersible PEG surface modified ultra small superparamagnetic iron oxide nanoparticles useful for target-specific biomedical applications. *Nanotechnology* **2008**, *19*, 365603. [CrossRef]
46. Kumar, A.; Pandey, A.K.; Singh, S.S.; Shanker, R.; Dhawan, A. Cellular uptake and mutagenic potential of metal oxide nanoparticles in bacterial cells. *Chemosphere* **2011**, *83*, 1124–1132. [CrossRef] [PubMed]
47. Alphandéry, E. Biodistribution and targeting properties of iron oxide nanoparticles for treatments of cancer and iron anemia disease. *Nanotoxicology* **2019**, *13*, 573–596. [CrossRef]
48. Soares, G.; Próspero, A.; Calabresi, M.; Rodrigues, D.; Simoes, L.; Quini, C.; Matos, R.; Pinto, L.; Sousa, A.; Bakuzis, A. Multichannel AC Biosusceptometry system to map biodistribution and assess the pharmacokinetic profile of magnetic nanoparticles by imaging. *IEEE Trans. Nanobiosci.* **2019**, *18*, 456–462. [CrossRef]
49. Zhang, Y.-N.; Poon, W.; Tavares, A.J.; McGilvray, I.D.; Chan, W.C. Nanoparticle–liver interactions: Cellular uptake and hepatobiliary elimination. *J. Control. Release* **2016**, *240*, 332–348. [CrossRef]
50. Cole, A.J.; David, A.E.; Wang, J.; Galbán, C.J.; Yang, V.C. Magnetic brain tumor targeting and biodistribution of long-circulating PEG-modified, cross-linked starch-coated iron oxide nanoparticles. *Biomaterials* **2011**, *32*, 6291–6301. [CrossRef]
51. Duguet, E.; Vasseur, S.; Mornet, S.; Devoisselle, J.M. Magnetic nanoparticles and their applications in medicine. *Nanomedicine* **2006**, *1*, 157–168. [CrossRef]
52. Maurea, S.; Mainenti, P.P.; Tambasco, A.; Imbriaco, M.; Mollica, C.; Laccetti, E.; Camera, L.; Liuzzi, R.; Salvatore, M. Diagnostic accuracy of MR imaging to identify and characterize focal liver lesions: Comparison between gadolinium and superparamagnetic iron oxide contrast media. *Quant. Imaging Med. Surg.* **2014**, *4*, 181.
53. Lurie, Y.; Webb, M.; Cytter-Kuint, R.; Shteingart, S.; Lederkremer, G.Z. Non-invasive diagnosis of liver fibrosis and cirrhosis. *World J. Gastroenterol.* **2015**, *21*, 11567–11583. [CrossRef]
54. Faria, S.C.; Ganesan, K.; Mwangi, I.; Shiehmorteza, M.; Viamonte, B.; Mazhar, S.; Peterson, M.; Kono, Y.; Santillan, C.; Casola, G. MR imaging of liver fibrosis: Current state of the art. *Radiographics* **2009**, *29*, 1615–1635. [CrossRef] [PubMed]
55. Petitclerc, L.; Sebastiani, G.; Gilbert, G.; Cloutier, G.; Tang, A. Liver fibrosis: Review of current imaging and MRI quantification techniques. *J. Magn. Reson. Imaging* **2017**, *45*, 1276–1295. [CrossRef] [PubMed]
56. Alphandéry, E.J.R.a. Iron oxide nanoparticles as multimodal imaging tools. *RSC Adv.* **2019**, *9*, 40577–40587. [CrossRef] [PubMed]
57. Zheng, B.; Vazin, T.; Goodwill, P.W.; Conway, A.; Verma, A.; Ulku Saritas, E.; Schaffer, D.; Conolly, S.M.J.S.r. Magnetic particle imaging tracks the long-term fate of in vivo neural cell implants with high image contrast. *Sci. Rep.* **2015**, *5*, 14055. [CrossRef] [PubMed]
58. Madru, R.; Kjellman, P.; Olsson, F.; Wingårdh, K.; Ingvar, C.; Ståhlberg, F.; Olsrud, J.; Lätt, J.; Fredriksson, S.; Knutsson, L.; et al. 99mTc-labeled superparamagnetic iron oxide nanoparticles for multimodality SPECT/MRI of sentinel lymph nodes. *J. Nucl. Med.* **2012**, *53*, 459–463. [CrossRef] [PubMed]
59. Forte, E.; Fiorenza, D.; Torino, E.; Costagliola di Polidoro, A.; Cavaliere, C.; Netti, P.A.; Salvatore, M.; Aiello, M. Radiolabeled PET/MRI Nanoparticles for Tumor Imaging. *J. Clin. Med.* **2019**, *9*, 89. [CrossRef]
60. Shen, S.; Wang, S.; Zheng, R.; Zhu, X.; Jiang, X.; Fu, D.; Yang, W. Magnetic nanoparticle clusters for photothermal therapy with near-infrared irradiation. *Biomaterials* **2015**, *39*, 67–74. [CrossRef]
61. Seested, T.; Appa, R.S.; Christensen, E.I.; Ioannou, Y.A.; Krogh, T.N.; Karpf, D.M.; Nielsen, H.M. In vivo clearance and metabolism of recombinant activated factor VII (rFVIIa) and its complexes with plasma protease inhibitors in the liver. *Thromb. Res.* **2011**, *127*, 356–362. [CrossRef]

62. Levy, M.; Luciani, N.; Alloyeau, D.; Elgrabli, D.; Deveaux, V.; Pechoux, C.; Chat, S.; Wang, G.; Vats, N.; Gendron, F.; et al. Long term in vivo biotransformation of iron oxide nanoparticles. *Biomaterials* **2011**, *32*, 3988–3999. [CrossRef]
63. Soares, G.A.; Pires, D.W.; Pinto, L.A.; Rodrigues, G.S.; Prospero, A.G.; Biasotti, G.G.A.; Bittencourt, G.N.; Stoppa, E.G.; Corá, L.A.; Oliveira, R.B.; et al. The Influence of Omeprazole on the Dissolution Processes of pH-Dependent Magnetic Tablets Assessed by Pharmacomagnetography. *Pharmaceutics* **2021**, *13*, 1274. [CrossRef]
64. Soares, G.A.; Faria, J.V.C.; Pinto, L.A.; Prospero, A.G.; Pereira, G.M.; Stoppa, E.G. Long-Term Clearance and Biodistribution of Magnetic Nanoparticles Assessed by AC Biosusceptometry. *Materials* **2022**, *15*, 2121. [CrossRef]
65. Prospero, A.G.; Buranello, L.P.; Fernandes, C.A.; Dos Santos, L.D.; Soares, G.; Rossini, B.C.; Zufelato, N.; Bakuzis, A.F.; de Mattos Fontes, M.R.; de Arruda Miranda, J.R. Corona protein impacts on alternating current biosusceptometry signal and circulation times of differently coated $MnFe_2O_4$ nanoparticles. *Nanomedicine* **2021**, *16*, 2189–2206. [CrossRef]
66. Prospero, A.G.; Fidelis-de-Oliveira, P.; Soares, G.A.; Miranda, M.F.; Pinto, L.A.; Dos Santos, D.C.; Silva, V.D.S.; Zufelato, N.; Bakuzis, A.F.; Miranda, J.R. AC biosusceptometry and magnetic nanoparticles to assess doxorubicin-induced kidney injury in rats. *Nanomedicine* **2020**, *15*, 511–525. [CrossRef]
67. Quini, C.C.; Prospero, A.G.; Calabresi, M.F.F.; Moretto, G.M.; Zufelato, N.; Krishnan, S.; Pina, D.R.; Oliveira, R.B.; Baffa, O.; Bakuzis, A.F.; et al. Real-time liver uptake and biodistribution of magnetic nanoparticles determined by AC biosusceptometry. *Nanomedicine* **2017**, *13*, 1519–1529. [CrossRef]
68. Biasotti, G.G.d.A.; Próspero, A.G.; Alvarez, M.D.T.; Liebl, M.; Pinto, L.A.; Soares, G.A.; Bakuzis, A.F.; Baffa, O.; Wiekhorst, F.; Miranda, J.R.d.A. 2D Quantitative Imaging of Magnetic Nanoparticles by an AC Biosusceptometry Based Scanning Approach and Inverse Problem. *Sensors* **2021**, *21*, 7063.
69. Branquinho, L.C.; Carriao, M.S.; Costa, A.S.; Zufelato, N.; Sousa, M.H.; Miotto, R.; Ivkov, R.; Bakuzis, A.F. Effect of magnetic dipolar interactions on nanoparticle heating efficiency: Implications for cancer hyperthermia. *Sci. Rep.* **2013**, *3*, 2887. [CrossRef]
70. Nunes, A.D.; Gomes-Silva, L.A.; Zufelato, N.; Próspero, A.G.; Quini, C.C.; Matos, R.V.; Miranda, J.R.; Bakuzis, A.F.; Castro, C.H. Albumin coating prevents cardiac effect of the magnetic nanoparticles. *IEEE Trans. Nanobiosci.* **2019**, *18*, 640–650. [CrossRef]
71. Tatematsu, M.; Tsuda, H.; Shirai, T.; Masui, T.; Ito, N.J.T.P. Placental glutathione S-transferase (GST-P) as a new marker for hepatocarcinogenesis: In vivo short-term screening for hepatocarcinogens. *Toxicol. Pathol.* **1987**, *15*, 60–68. [CrossRef]
72. Chistiakov, D.A.; Killingsworth, M.C.; Myasoedova, V.A.; Orekhov, A.N.; Bobryshev, Y.V. CD68/macrosialin: Not just a histochemical marker. *Lab. Investig.* **2017**, *97*, 4–13. [CrossRef]
73. Ishak, K. Histological grading and staging of chronic hepatitis. *J. Hepatol.* **1995**, *22*, 696–699. [CrossRef]
74. Sousa-Junior, A.A.; Mendanha, S.A.; Carrião, M.S.; Capistrano, G.; Próspero, A.G.; Soares, G.A.; Cintra, E.R.; Santos, S.F.O.; Zufelato, N.; Alonso, A.; et al. Predictive Model for Delivery Efficiency: Erythrocyte Membrane-Camouflaged Magnetofluorescent Nanocarriers Study. *Mol. Pharm.* **2020**, *17*, 837–851. [CrossRef]
75. Islam, K.; Haque, M.; Kumar, A.; Hoq, A.; Hyder, F.; Hoque, S.M. Manganese ferrite nanoparticles ($MnFe_2O_4$): Size dependence for hyperthermia and negative/positive contrast enhancement in MRI. *Nanomaterials* **2020**, *10*, 2297. [CrossRef]
76. Jardim, K.V.; Palomec-Garfias, A.F.; Andrade, B.Y.G.; Chaker, J.A.; Báo, S.N.; Márquez-Beltrán, C.; Moya, S.E.; Parize, A.L.; Sousa, M.H. Novel magneto-responsive nanoplatforms based on $MnFe_2O_4$ nanoparticles layer-by-layer functionalized with chitosan and sodium alginate for magnetic controlled release of curcumin. *Mater. Sci. Eng. C* **2018**, *92*, 184–195. [CrossRef]
77. Darwish, M.S.; Stibor, I. Pentenoic acid-stabilized magnetic nanoparticles for nanomedicine applications. *J. Dispers. Sci. Technol.* **2016**, *37*, 1793–1798. [CrossRef]
78. Chertok, B.; David, A.E.; Yang, V.C. Polyethyleneimine-modified iron oxide nanoparticles for brain tumor drug delivery using magnetic targeting and intra-carotid administration. *Biomaterials* **2010**, *31*, 6317–6324. [CrossRef]
79. Sakulkhu, U.; Mahmoudi, M.; Maurizi, L.; Salaklang, J.; Hofmann, H. Protein corona composition of superparamagnetic iron oxide nanoparticles with various physico-chemical properties and coatings. *Sci. Rep.* **2014**, *4*, 5020. [CrossRef]
80. Feng, Q.; Liu, Y.; Huang, J.; Chen, K.; Huang, J.; Xiao, K. Uptake, distribution, clearance, and toxicity of iron oxide nanoparticles with different sizes and coatings. *Sci. Rep.* **2018**, *8*, 2082. [CrossRef]
81. Gupta, A.K.; Naregalkar, R.R.; Vaidya, V.D.; Gupta, M. Recent advances on surface engineering of magnetic iron oxide nanoparticles and their biomedical applications. *Future Med.* **2007**, *2*, 23–29. [CrossRef]
82. Han, S.S.; Li, Z.Y.; Zhu, J.Y.; Han, K.; Zeng, Z.Y.; Hong, W.; Li, W.X.; Jia, H.Z.; Liu, Y.; Zhuo, R.X.J.S. Dual-pH sensitive charge-reversal polypeptide micelles for tumor-triggered targeting uptake and nuclear drug delivery. *Small* **2015**, *11*, 2543–2554. [CrossRef] [PubMed]
83. Kenzaoui, B.H.; Vilà, M.R.; Miquel, J.M.; Cengelli, F.; Juillerat-Jeanneret, L. Evaluation of uptake and transport of cationic and anionic ultrasmall iron oxide nanoparticles by human colon cells. *Int. J. Nanomed.* **2012**, *7*, 1275.
84. Petri-Fink, A.; Chastellain, M.; Juillerat-Jeanneret, L.; Ferrari, A.; Hofmann, H. Development of functionalized superparamagnetic iron oxide nanoparticles for interaction with human cancer cells. *Biomaterials* **2005**, *26*, 2685–2694. [CrossRef] [PubMed]
85. Xiao, K.; Li, Y.; Luo, J.; Lee, J.S.; Xiao, W.; Gonik, A.M.; Agarwal, R.G.; Lam, K.S. The effect of surface charge on in vivo biodistribution of PEG-oligocholic acid based micellar nanoparticles. *Biomaterials* **2011**, *32*, 3435–3446. [CrossRef]
86. Imam, S.Z.; Lantz-McPeak, S.M.; Cuevas, E.; Rosas-Hernandez, H.; Liachenko, S.; Zhang, Y.; Sarkar, S.; Ramu, J.; Robinson, B.L.; Jones, Y.; et al. Iron oxide nanoparticles induce dopaminergic damage: In vitro pathways and in vivo imaging reveals mechanism of neuronal damage. *Mol. Neurobiol.* **2015**, *52*, 913–926. [CrossRef]

87. Elbialy, N.S.; Aboushoushah, S.F.; Alshammari, W.W. Long-term biodistribution and toxicity of curcumin capped iron oxide nanoparticles after single-dose administration in mice. *Life Sci.* **2019**, *230*, 76–83. [CrossRef]
88. Rodrigues, H.F.; Mello, F.M.; Branquinho, L.C.; Zufelato, N.; Silveira-Lacerda, E.P.; Bakuzis, A.F. Real-time infrared thermography detection of magnetic nanoparticle hyperthermia in a murine model under a non-uniform field configuration. *Int. J. Hyperth.* **2013**, *29*, 752–767. [CrossRef]
89. Wilhelm, S.; Tavares, A.J.; Dai, Q.; Ohta, S.; Audet, J.; Dvorak, H.F.; Chan, W.C.J.N.r.m. Analysis of nanoparticle delivery to tumours. *Nat. Rev. Mater.* **2016**, *1*, 16014. [CrossRef]
90. Tavares, A.J.; Poon, W.; Zhang, Y.-N.; Dai, Q.; Besla, R.; Ding, D.; Ouyang, B.; Li, A.; Chen, J.; Zhang, Y.N.; et al. Effect of removing Kupffer cells on nanoparticle tumor delivery. *Proc. Natl. Acad. Sci. USA* **2017**, *114*, E10871–E10880. [CrossRef]
91. Li, L.; Wei, W.; Li, Z.; Chen, H.; Li, Y.; Jiang, W.; Chen, W.; Kong, G.; Yang, J.; Li, Z. The Spleen Promotes the Secretion of CCL2 and Supports an M1 Dominant Phenotype in Hepatic Macrophages During Liver Fibrosis. *Cell. Physiol. Biochem.* **2018**, *51*, 557–574. [CrossRef]
92. Li, L.; Duan, M.; Chen, W.; Jiang, A.; Li, X.; Yang, J.; Li, Z. The spleen in liver cirrhosis: Revisiting an old enemy with novel targets. *J. Transl. Med.* **2017**, *15*, 111. [CrossRef]
93. Murotomi, K.; Arai, S.; Uchida, S.; Endo, S.; Mitsuzumi, H.; Tabei, Y.; Yoshida, Y.; Nakajima, Y. Involvement of splenic iron accumulation in the development of nonalcoholic steatohepatitis in Tsumura Suzuki Obese Diabetes mice. *Sci. Rep.* **2016**, *6*, 22476. [CrossRef]
94. Wei, Y.; Zhao, M.; Yang, F.; Mao, Y.; Xie, H.; Zhou, Q. Iron overload by Superparamagnetic Iron Oxide Nanoparticles is a High Risk Factor in Cirrhosis by a Systems Toxicology Assessment. *Sci. Rep.* **2016**, *6*, 29110. [CrossRef]
95. Han, X.; Lv, Y.; Li, Y.; Deng, J.; Qiu, Q.; Liu, N.; Zhao, S.; Liao, C. Distribution characteristics of cells in splenomegaly due to hepatitis B-related cirrhotic portal hypertension and their clinical importance. *J. Int. Med. Res.* **2018**, *46*, 2633–2640. [CrossRef]
96. Ergen, C.; Niemietz, P.M.; Heymann, F.; Baues, M.; Gremse, F.; Pola, R.; van Bloois, L.; Storm, G.; Kiessling, F.; Trautwein, C.; et al. Liver fibrosis affects the targeting properties of drug delivery systems to macrophage subsets in vivo. *Biomaterials* **2019**, *206*, 49–60. [CrossRef]
97. Hundt, W.; Petsch, R.; Helmberger, T.; Reiser, M. Signal changes in liver and spleen after Endorem administration in patients with and without liver cirrhosis. *Eur. Radiol.* **2000**, *10*, 409–416. [CrossRef]
98. Borst, K.; Frenz, T.; Spanier, J.; Tegtmeyer, P.-K.; Chhatbar, C.; Skerra, J.; Ghita, L.; Namineni, S.; Lienenklaus, S.; Köster, M. Type I interferon receptor signaling delays Kupffer cell replenishment during acute fulminant viral hepatitis. *J. Hepatol.* **2018**, *68*, 682–690. [CrossRef]
99. Borst, K.; Graalmann, T.; Kalinke, U. Reply to: "Lack of Kupffer cell depletion in diethylnitrosamine-induced hepatic inflammation". *J. Hepatol.* **2019**, *70*, 815–816. [CrossRef]
100. Kessler, S.M.; Hoppstädter, J.; Hosseini, K.; Laggai, S.; Haybaeck, J.; Kiemer, A.K. Lack of Kupffer cell depletion in diethylnitrosamine-induced hepatic inflammation. *J. Hepatol.* **2019**, *70*, 813–815. [CrossRef]
101. Sanz-García, C.; Fernández-Iglesias, A.; Gracia-Sancho, J.; Arráez-Aybar, L.A.; Nevzorova, Y.A.; Cubero, F.J. The Space of Disse: The Liver Hub in Health and Disease. *Livers* **2021**, *1*, 3–26. [CrossRef]
102. Ni, Y.; Li, J.-M.; Liu, M.-K.; Zhang, T.-T.; Wang, D.-P.; Zhou, W.-H.; Hu, L.-Z.; Lv, W.-L. Pathological process of liver sinusoidal endothelial cells in liver diseases. *World J. Gastroenterol.* **2017**, *23*, 7666–7677. [CrossRef] [PubMed]
103. Cheng, Q.-N.; Yang, X.; Wu, J.-F.; Ai, W.-B.; Ni, Y.-R. Interaction of non-parenchymal hepatocytes in the process of hepatic fibrosis. *Mol. Med. Rep.* **2021**, *23*, 364. [CrossRef] [PubMed]
104. Lafoz, E.; Ruart, M. The Endothelium as a Driver of Liver Fibrosis and Regeneration. *Cells* **2020**, *9*, 929. [CrossRef] [PubMed]
105. Sun, T.; Kang, Y.; Liu, J.; Zhang, Y.; Ou, L.; Liu, X.; Lai, R.; Shao, L. Nanomaterials and hepatic disease: Toxicokinetics, disease types, intrinsic mechanisms, liver susceptibility, and influencing factors. *J. Nanobiotechnol.* **2021**, *19*, 108. [CrossRef]
106. De Rudder, M.; Dili, A.; Stärkel, P.; Leclercq, I.A. Critical Role of LSEC in Post-Hepatectomy Liver Regeneration and Failure. *Int. J. Mol. Sci* **2021**, *22*, 8053. [CrossRef]
107. Iwakiri, Y.; Trebicka, J. Portal hypertension in cirrhosis: Pathophysiological mechanisms and therapy. *JHEP Rep. Innov. Hepatol.* **2021**, *3*, 100316. [CrossRef]
108. Hall, A.; Cotoi, C.; Luong, T.V.; Watkins, J.; Bhathal, P.; Quaglia, A. Collagen and elastic fibres in acute and chronic liver injury. *Sci. Rep.* **2021**, *11*, 14569. [CrossRef]
109. Soulaidopoulos, S.; Cholongitas, E.; Giannakoulas, G.; Vlachou, M.; Goulis, I. Review article: Update on current and emergent data on hepatopulmonary syndrome. *World J. Gastroenterol.* **2018**, *24*, 1285–1298. [CrossRef]
110. Cheng, T.-Y.; Lee, W.-S.; Huang, H.-C.; Lee, F.-Y.; Chang, C.-C.; Lin, H.-C.; Lee, S.-D. The effects of pioglitazone in cirrhotic rats with hepatopulmonary syndrome. *J. Chin. Med. Assoc.* **2017**, *80*, 683–689. [CrossRef]
111. Nuzzo, A.; Dautry, R.; Francoz, C.; Logeart, D.; Mégarbane, B. Hepatopulmonary syndrome-attributed extreme hypoxemia and polycythemia revealing liver cirrhosis. *Am. J. Emerg. Med.* **2019**, *37*, 175.e171–175.e172. [CrossRef]
112. Jiang, L.-Q.; Wang, T.-Y.; Wang, Y.; Wang, Z.-Y.; Bai, Y.-T. Co-disposition of chitosan nanoparticles by multi types of hepatic cells and their subsequent biological elimination: The mechanism and kinetic studies at the cellular and animal levels. *Int. J. Nanomed.* **2019**, *14*, 6035–6060. [CrossRef]

CONCLUSÃO GERAL

A tese apresentada concebeu dois trabalhos desenvolvidos no doutorado do aluno. Através dos resultados apresentados nos capítulos II e III, é possível concluir que as NPMs evidentemente tendem a se depositar no fígado. Ainda de forma geral, é notável que as NPMs têm um significante potencial de na clínica média, contudo estudos como esses desenvolvidos ainda se mostram essenciais, uma vez que podem auxiliar como alcançar e explorar todas as vantagens.

O primeiro trabalho revelou que as NPMs podem ser encontradas até 60 dias após a administração, apesar de apresentar um decréscimo significativo. Os dados indicaram que as NPMs utilizadas demonstraram uma taxa de eliminação constante a partir de 48 h via fezes, fato esse que pode auxiliar na compreensão de como materiais nanoestruturados são eliminados, considerando o crescimento acentuado de fármacos baseado em nanotecnologia. Além disso, o estudo demonstrou que eliminação de NPMs não é um processo trivial, visto que mecanismos endógenos de metabolização ou possível processo aglomeração das NPMs ocorrem.

O trabalho direcionado a avaliação da função hepática sob a influência da cirrose demonstrou o fígado é efetivamente afetado por essa condição. O estudo farmacocinético de maneira geral indicou um menor acumulo de NPMs no fígado cirrótico. Os resultados foram sustentados pela hipótese que fluxo sanguíneo que atinge os hepatócitos, devido a capilarização dos sinusóides hepáticos. Acredita-se que os resultados obtidos são validos para elucidar interação de nanopartículas com o tecido hepático, o que pode favorecer o desenvolvimento de novas estratégias para direcionadas a entrega de drogas ao tecido hepático.

Ambos os trabalhos permitiram visualizar que o sistema BAC se consolida ao longo dos anos como uma ferramenta eficaz para detectar e monitorar NPM, seja de forma dinâmica através de imagens ou até mesmo em protocolos de quantificação *ex vivo.* A versatilidade é a principal característica do sistema, o que destaca sua habilidade em associação com materiais magnéticos e até mesmo outras técnicas. Além disso, a versatilidade confere ao sistema a habilidade de se executar avanços instrumentais e metodológicos, favorecendo a continuidade em sua utilização em diversas áreas.